

# Magnetic signatures on mixed-mode frequencies

## II. Period spacings as a probe of the internal magnetism of red giants

L. Bugnet

Flatiron Institute, Simons Foundation, 162 Fifth Ave, New York, NY 10010, USA,  
e-mail: lbugnet@flatironinstitute.org

Received 21 January 2022 / Accepted 24 August 2022

### ABSTRACT

*Context.* Theoretical works have looked into the various topologies and amplitudes, as well as the stability of the magnetic field that is expected to be present in the radiative interior of stars evolving after the main sequence. From these studies, we know that strong stable "fossil" fields might be trapped inside evolved stars. These could trigger the strong transport of angular momentum from the core to the envelope, a process that is not generally included in state-of-the-art stellar models. This may therefore have a substantial impact on the mixing and the inferred stellar parameters. Such internal magnetic fields have never been observed in evolved stars. As a result, there is a major piece missing from our global picture of stars as dynamical bodies.

*Aims.* Asteroseismology has opened a window onto stellar internal dynamics, as oscillation frequencies, amplitudes, and lifetimes are affected by processes that are taking place inside the star. The detection of buried magnetic fields could therefore be possible through the measurement of their impact on the oscillations of stars. This advancement would be groundbreaking for our knowledge of stellar dynamics. In this scope, magnetic signatures on mixed-mode frequencies have recently been characterized, but the task of detection remains challenging as the mixed-mode frequency pattern is highly complex and affected by rotational effects, while modes of different radial orders are often intertwined. In this work, we aim to build a bridge between theoretical prescriptions and complex asteroseismic data analysis to facilitate a future search and characterization of internal magnetism with asteroseismology.

*Methods.* We investigated the effect of magnetic fields inside evolved stars with solar-like oscillations on the estimation of the period spacing of gravity-mode (g-mode) components of simulated mixed gravito-acoustic modes. We derived a new corrected stretching function of the power spectrum density to account for the presence of magnetic signatures on their frequencies.

*Results.* We demonstrate that the strong dependency of the amplitude of the magnetic signature with mixed-mode frequencies leads to biased estimates of period spacings towards lower values. We also show that a careful analysis of the oscillation frequency pattern through various period spacing estimates and across a broad frequency range might lead to the first detection of magnetic fields inside red giants and at the same time, we adjust the measured value of g-mode period spacing.

**Key words.** Asteroseismology - stars: oscillations - stars: magnetic field - stars: interiors - stars: evolution - stars: rotation

### 1. Introduction

Unveiling the internal dynamical processes taking place within stellar interiors is one of the challenges related to the revolution in asteroseismology revolution over the past ten years (Aerts et al. 2019). It is of paramount importance to achieve realistic modelings of the internal transport of angular momentum (AM) and mixing of chemical elements to compute robust evolutionary tracks (Eggenberger 2015), as well as to estimate stellar ages (Lebreton et al. 2014) in an accurate way. The *Kepler* mission (Borucki et al. 2008) carried out observations of stars along their evolutionary tracks over four continuous years. This observing duration is large enough to allow the detection of very detailed patterns in the frequency domain, where stellar oscillations are studied. Asteroseismology recently allowed the measurement of the internal rotation rate of subgiants (SG, e.g., Deheuvels et al. 2012, 2014, 2016, 2020) and red giants (RG, e.g., Beck et al. 2012, 2014; Mosser et al. 2012b, 2015, 2018; Vrad et al. 2016; Di Mauro et al. 2016; Triana et al. 2017; Gehan et al. 2018; Tayar et al. 2019; see Aerts et al. 2019 for a summary). These rotation-rate measurements point out a major discrepancy, namely, of two orders of magnitude, between the observed rotation rates and the much larger ones

obtained through state-of-the-art stellar modeling (Ceillier et al. 2012; Marques et al. 2013; Eggenberger et al. 2012, 2019a,b). Therefore, there must be at least one process that would be efficient enough to transport angular momentum from the deepest layers of the star to the surface, which has not yet been taken into account in our current knowledge of stellar dynamics. This is despite the fact that numerous transport processes have been investigated to try and fill in the picture of stellar dynamics (Mathis 2013; Aerts et al. 2019):

First, stellar model physics already includes rotation and associated hydrodynamical transport processes (meridional circulation or shear instabilities, e.g., Zahn 1992; Maeder & Zahn 1998; Mathis & Zahn 2004; Mathis et al. 2004, 2018), whose present characterizations do not include the observed low internal rotation rates of stellar cores or weak core-to-surface differential rotation among their effects. The shear (Zahn 1992; Maeder & Meynet 1996; Talon & Zahn 1997; Mathis et al. 2004, 2018) or the Goldreich-Schubert-Fricke (Barker et al. 2019) instabilities are known to transport AM, but the expected effects are too weak for either of them to fully explain the observed rotation rates of solar-like stars (Marques et al. 2013).

Second, mixed acoustic-gravity oscillation modes (Belkacem et al. 2015) efficiently transport angular momentum during the RG phase, but their effect is too weak on the SG phase, where strong angular momentum transport is expected. On the contrary, internal gravity waves (Talon & Charbonnel 2008; Pinçon et al. 2017) are efficient in the early stages of evolution, but fail to transport AM during the red giant branch (RGB, Fuller et al. 2014).

Next, Tayler (1973) suggested that a magneto-hydrodynamic instability might occur in radiative zones and Spruit (2002) has demonstrated that the instability might cause a "Tayler-Spruit" dynamo. The physical existence of such magnetic dynamos has been debated by Zahn et al. (2007), leading Fuller et al. (2019) and Eggenberger et al. (2019c) to investigate the effect of the instability itself (without the dynamo loop) on the AM transport inside RGs. The efficiency of the Maxwell stresses on transporting AM is in good agreement with observations, but this instability cannot simultaneously solve the AM transport problem in SGs and RGs (Eggenberger et al. 2019b,c).

Finally, stable magnetic fields tend to homogenize rotation along the field lines (Mestel & Weiss 1987; Gough & Thompson 1990; Brun & Zahn 2006; Strugarek et al. 2011; Acevedo-Arreguin et al. 2013; Kissin & Thompson 2015), which could result in a highly efficient AM transport. Such stable fossil fields are observed at the surface of  $\sim 10\%$  of intermediate-mass stars on the main sequence (MS, e.g., Donati & Landstreet 2009). Inside RGs, magnetic fields could result from past dynamo action during the pre-main sequence (PMS) or MS and remain trapped inside the radiative interior of solar-like stars for the rest of their evolution (MacGregor & Cassinelli 2003; see the discussion on the magnetic scenario in Bugnet et al. 2021).

In this work, we proceed under the hypothesis that stars possess magnetized stellar radiative interiors during the advanced stages of their evolution, namely, after the MS. We focus on red giant stars that present "solar-like oscillations" with visible mixed gravito-acoustic dipolar modes. This is the case for stars on the SG phase on the RGB, and the first and second clumps. The only window we might have on internal magnetism is magneto-asteroseismology (Neiner et al. 2015; Mathis et al. 2021), which consists of a search for characteristic signatures of magnetic fields in the observed frequency spectra of stellar oscillations. So far, only a few magneto-asteroseismology analyses have been performed, namely, for the Sun (Goode & Thompson 1992; Kiefer & Roth 2018) and for early-type stars (Takata & Shibahashi 1994; Shibahashi & Aerts 2000). Recent theoretical works on evolved stars (red giants, Bugnet et al. 2021; Mathis et al. 2021; Loi 2020, 2021) have paved the way for observational studies of magnetism inside evolved stars. Fuller et al. (2015) (and later Loi & Papaloizou 2017; Lecoanet et al. 2017) demonstrated that low-frequency internal gravity waves might be converted into Alfvén waves in the presence of strong magnetic fields. As a result, classical mixed acoustic gravity modes (*g*-modes) might not form inside magnetized red giants. This process could impact the amplitudes of the observed dipolar and quadrupolar mixed modes and may then justify the large fraction of observed intermediate-mass stars on the RGB showing abnormally low non-radial oscillation amplitudes (Mosser et al. 2012a; García et al. 2014; Stello et al. 2016a,b). To prove or disprove the hypothesis of magnetized radiative interiors and the resulting observations, recent studies have focused on the theoretical impact of stable fossil fields on mixed-mode frequencies. Among them, Bugnet et al. (2021) demonstrated that the effect of the expected stable magnetic configuration (axisymmetric, aligned with the rotation axis of the star) on mixed-mode

frequencies is large enough to allow detections in *Kepler* data. Mathis et al. (2021) provided the theoretical framework needed to perform radial magnetic-field inversions from observed magnetic frequency perturbations. This prescription would be game-changing for the characterization of magnetic fields in the case of detections of frequency perturbations in asteroseismic data. Loi (2021) completed the theoretical picture of the effect of fossil fields on the mixed-mode frequency pattern by considering the effect of the field inclination on the magnetic signature, similarly to the study of Goode & Thompson (1992).

Despite all this recent progress in terms of theoretical study, the internal magnetic fields of RGs have not yet been detected. Such detections require a very detailed analysis of individual mode frequencies, which is even more challenging than recent studies that have allowed for the measurement of RG core rotation rates (Vrard et al. 2016; Mosser et al. 2018; Gehan et al. 2018). Thus, the search for internal magnetism requires more guidance. This study is aimed at building a bridge between theoretical predictions and the complexity and challenges related to asteroseismic observables.

Mixed modes result from a coupling between acoustic modes (*p*-modes) that are evenly spaced in frequency and gravity modes (*g*-modes) in the radiative interior that are evenly spaced in terms of period (e.g., Dupret et al. 2009). A characteristic frequency spacing ( $\Delta\nu$ ) is associated with the acoustic pattern and a characteristic period spacing (defined as the distance in period between two consecutive *g*-modes with the same horizontal order and consecutive radial orders  $\Delta\Pi_1$ , Beck et al. 2011) is associated with pure *g*-modes. The *g*-mode period spacing can be measured from asteroseismic observation (e.g., Mosser et al. 2015; Vrard et al. 2016; Buysschaert et al. 2016) and its value reflects the inner structure of the star along its evolution (Bedding et al. 2011; Mosser et al. 2012c; Stello et al. 2013).

In Section 2, we provide the physical background required to generate artificial RG frequency patterns on which we base this work. In Section 3, we use this typical RG frequency pattern to investigate the effect of a fossil stable magnetic field in the radiative interior on the determination of the *g*-mode period spacing. In Section 4, we demonstrate that magnetic signatures could possibly be detected thanks to the effect they induce on the observed *g*-mode period spacing. We discuss results in Sect. 5. In Sect. 6, we conclude with an observational perspective on this work.

## 2. Measurement of the *g*-mode period spacing

The objective of this study is to investigate the detectability of an axisymmetric magnetic field inside the radiative interior of evolved stars with solar-like oscillations from the measurement of the period spacing between pure *g*-modes (hereafter noted  $\Delta\Pi_1$ ). To remain unbiased from observational interpretations, we base our study on simulated power spectral densities (PSD) of RGB stars through a magnetic adaptation of the *sloscillations*<sup>1</sup> pipeline (Kuszlewicz et al. 2019) thanks to the prescriptions of Bugnet et al. (2021) and Mathis et al. (2021).

<sup>1</sup> <https://github.com/jsk389/sloscillations>

## 2.1. Building synthetic asteroseismic power spectrum densities

In this section, we provide the physical context and equations needed to build a realistic red-giant synthetic PSD and we rely on existing methods to extract the stellar seismic parameters of interest,  $\Delta\Pi_1$ , from an asteroseismic analysis.

### 2.1.1. Mixed-mode frequencies

The second-order asymptotic expression for pure p-modes allows for an estimation of the frequencies of radial ( $\ell = 0$ ), dipolar ( $\ell = 1$ ), and quadrupolar ( $\ell = 2$ ) modes following Mosser et al. (2011). The asymptotic expression for dipolar-mode eigenfrequencies reads (Tassoul 1980):

$$\nu_{p,\ell=1} = \left( n_p + \frac{1}{2} + \epsilon_p - d_{01} + \frac{\alpha}{2} (n_p - n_{\max})^2 \right) \Delta\nu, \quad (1)$$

with  $\nu_{p,\ell=1}$  as the theoretical frequency of pure pressure modes,  $\Delta\nu$  as the frequency separation due to pressure modes of consecutive radial orders,  $n_p$  as the radial order of the pure pressure mode,  $\epsilon_p$  as the acoustic offset,  $n_{\max} = \frac{\nu_{\max}}{\Delta\nu} - \epsilon_p$  as the order corresponding to the p- $m$  mode closest to  $\nu_{\max}$ ,  $\alpha = 0.015\Delta\nu^{-0.32}$  (Mosser et al. 2013; Vrad et al. 2016), and  $d_{01} = 0.0553 - 0.036 \log \Delta\nu$ , as measured from stars on the RGB by Mosser et al. (2014, 2018).

The structure of stars evolving as giants after the end of the main sequence allows interval gravity waves, propagating in the radiative core, to couple with the acoustic waves to form stationary mixed modes. Their theoretical frequencies are estimated following Mosser et al. (2012b) for dipolar so-called "mixed" modes as

$$\nu_{pg,\ell=1} = \nu_{p,\ell=1} + \frac{\Delta\nu}{\pi} \arctan \left[ q \tan \left[ \pi \left( \frac{1}{\Delta\Pi_1 \nu_{pg,\ell=1}} - \epsilon_g \right) \right] \right], \quad (2)$$

where  $\epsilon_g$  is the gravity offset and  $q$  is the coupling factor of mixed modes (Mosser et al. 2017b) estimated by combining the phases  $\theta_p$  and  $\theta_g$  of pressure- and gravity-wave contributions to mixed modes, following:

$$\tan \theta_p = q \tan \theta_g, \quad (3)$$

with

$$\theta_p = \pi \frac{\nu_{pg,\ell=1} - \nu_{p,\ell=1}}{\Delta\nu}, \quad (4)$$

and

$$\theta_g = \pi \frac{1}{\Delta\Pi_1} \left( \frac{1}{\nu_{pg,\ell=1}} - \frac{1}{\nu_{g,\ell=1}} \right). \quad (5)$$

In this study, we focus on dipolar mixed modes as they are the most sensitive to internal processes. We use the following notations:  $\nu$  to simplify the writing of the dipolar mixed-mode frequencies ( $\nu_{pg,\ell=1}$ ),  $\nu_p$  for the frequency of pure  $\ell = 1$  pressure modes ( $\nu_{p,\ell=1}$ ), and  $\nu_g$  for the frequency of pure  $\ell = 1$  g-modes ( $\nu_{g,\ell=1}$ ).

Using the elements introduced in Sections 2.1.1 and Appendix A, we can produce a synthetic oscillation-mode PSD of a typical RGB star with  $\nu_{\max} = 108.3 \mu\text{Hz}$ ,  $\Delta\nu = 10.84 \mu\text{Hz}$ , and  $\Delta\Pi_1 = 75.2$  seconds. The result is represented on the top panel of Fig. 1 by considering the typical observable frequency range  $[\nu_{\max} - 3\Delta\nu : \nu_{\max} + 3\Delta\nu]$ .

### 2.1.2. Mixed mode asymptotic behavior

Mixed-mode inertia can be dominated either by their acoustic component or by their gravity component, depending on their eigenfrequency. The nature of a mode can be measured from the comparison of the mode inertia (Goupil et al. 2013) in the radiative interior (mostly probed by g-modes) and the mode inertia in the convective envelope (mostly probed by p-modes). The ratio of the mode inertia in the radiative cavity on the total mode inertia defines the coupling function of mixed modes, expressed as (Goupil et al. 2013; Hekker et al. 2017):

$$\zeta = \left( 1 + \frac{q}{\mathcal{N}} \frac{1}{q^2 \cos^2 \theta_p + \sin^2 \theta_p} \right)^{-1}. \quad (6)$$

The value of the  $\zeta$  function is represented for each mixed mode of a simulated star on the RGB by the dots on each panel of Fig. 1. When the mode is purely acoustic ( $\theta_p = 0$ ), the  $\zeta$  function can be rewritten as:

$$\zeta_p = \zeta_{\min} = \left( 1 + \frac{\nu^2 \Delta\Pi_1}{q \Delta\nu} \right)^{-1}. \quad (7)$$

When the mode is a pure g-mode, ( $\theta_p = \frac{\pi}{2}$ ), we have:

$$\zeta_g = \zeta_{\max} = \left( 1 + \frac{q \nu^2 \Delta\Pi_1}{\Delta\nu} \right)^{-1}. \quad (8)$$

The maxima of the  $\zeta$  function therefore correspond to gravity-dominated (hereafter, g- $m$ ) modes, while dips are associated with acoustic-dominated (hereafter, p- $m$ ) modes. The g- $m$  modes are much more sensitive to internal processes than p- $m$  due to their relative inertia (Eq. 7). It is therefore convenient to focus on g- $m$  modes for the measurements of internal rotation rates, as done by Gehan et al. (2018). We applied the same methodology to prevent surface dynamical processes from biasing the search for buried magnetic fields and we focused the rest of our study on the g- $m$  modes localized near maxima of the zeta function. We then suppressed all modes contained in the range  $[\nu_{p_n} - 0.095\Delta\nu, \nu_{p_n} + 0.095\Delta\nu]$  around the nominal  $\nu_{p_n}$  frequency at each radial order  $n$  from the PSD before further analysis, as done by Gehan et al. (2018). Radial and quadrupolar modes are located in frequency ranges corresponding to g- $m$  dipolar modes. Thus, we also had to suppress their regions of the PSD for the measurement of  $\Delta\Pi_1$  to be accurate. For each radial order,  $n$ , we removed all the power in the frequency range of  $[\nu_{n,\ell=0} - 0.2\Delta\nu, \nu_{n,\ell=0} + 0.06\Delta\nu]$ , as done in Vrad et al. (2016). The PSDs used in the following are thus solely composed of g- $m$  dipolar modes away from radial and quadrupolar modes.

### 2.1.3. Stretched period spacing of mixed modes

While pure g-modes are evenly spaced in period, following:

$$\frac{1}{\nu_g} = (-n_g + \epsilon_g) \Delta\Pi_1, \quad (9)$$

the g-mode period spacing is affected by the coupling with p-modes, as shown by Eq. 2. We can deduce the period of mixed modes  $P$  as (Mosser et al. 2015):

$$\frac{dP}{dn} = -\zeta \Delta\Pi_1, \quad (10)$$

with  $n = n_p + n_g$  the order of mixed modes.

Equation 10 enhances the observation that, due to the coupling of the modes, mixed modes are not evenly spaced in period. To extract the periodicity of mixed modes, Vrad et al. (2016), Mosser et al. (2015), and Hekker et al. (2017) therefore defined the "stretched" period  $\pi$  via:

$$d\pi = -\frac{1}{\zeta} \frac{d\nu}{\nu^2}. \quad (11)$$

The pure g-modes period spacing is expressed as (Mosser et al. 2018):

$$\Delta\Pi_1 = -\int_{\nu_n}^{\nu_{n+1}} \frac{1}{\zeta} \frac{d\nu}{\nu^2}. \quad (12)$$

#### 2.1.4. Measurement of $\Delta\Pi_1$ and associated uncertainty

Vrad et al. (2016) measured the period spacing of g-modes by computing a Lomb-Scargle periodogram (LS periodogram, Lomb 1976; Scargle 1982) of the stretched PSD. Indeed, by stretching the original non-rotating, non-magnetized PSD onto the  $\pi$  variable defined by Eq. 11, the effect of the coupling of the modes on the observed frequencies through the  $\zeta$  function is removed (Vrad et al. 2016), and the periodicity of g-modes is unveiled in the  $\pi$ -stretched PSD. The periodicity,  $\Delta\Pi_1$ , is then measured from the period associated with the maximum power in the LS periodogram.

The measurement of  $\Delta\Pi_1$  from the stretching process is associated with various sources of uncertainties. We refer to Appendix A in the study of Vrad et al. (2016) for detailed discussions of all uncertainty sources in the measurement of this parameter from the LS method presented here. The resolution in the LS periodogram results is (in most cases) the main uncertainty contribution. Thus, this value has been used in most prior studies (Vrad et al. 2016; Gehan et al. 2018). The typical frequency of observed modes is  $\nu_{\max}$ , therefore, the LS periodogram has a resolution of  $\nu_{\max}$  around  $\Delta\Pi_1$ . The nominal resolution expressed in the period variable is written as (Vrad et al. 2016):

$$\delta(\Delta\Pi_1)_{\text{res}} = \nu_{\max} \Delta\Pi_1^2. \quad (13)$$

The typical resolution uncertainty is about 0.5 seconds on the RGB, representing a relative error of 1% in the measurement of  $\Delta\Pi_1$ . While this seems reasonable, an error in the estimate of  $\Delta\Pi_1$  of that order of magnitude would highly bias any search for signatures of internal dynamical processes. We performed an oversampling of the LS periodogram (by a factor of 6) to produce all results and figures in this article. This allowed us to get a more precise estimate of the location of the peak of maximum power, as demonstrated by Vrad et al. (2016). Following Mosser & Appourchaux (2009), we then use the oversampling resolution:

$$\delta(\Delta\Pi_{1,\text{over}}) = \frac{1.6}{A} \delta(\Delta\Pi_{1,\text{res}}). \quad (14)$$

As discussed in Vrad et al. (2016), typical dominant peak amplitudes  $A$  are largely above the threshold justifying much tighter resolution than the nominal resolution in the LS periodogram given by Eq. 13.

#### 2.2. Impact of the rotation on $\Delta\Pi_1$ measurements

To retrieve  $\Delta\Pi_1$  starting from an artificial PSD, we have to compute a LS periodogram of the  $\pi$ -stretched spectrum and to search for the period corresponding to the maximum amplitude in the LS periodogram. The orange curve in the top panel of Fig. 2 is an example of the measurement of  $\Delta\Pi_1$  from the LS periodogram built from Eq. 15 for a synthetic PSD representing a non-magnetized, non-rotating star inside which mixed-mode frequencies are not affected ( $\nu = \nu_{\text{obs}}$ ). The LS method applied to this star leads to a correct measurement of  $\Delta\Pi_{1,\text{LS}}$  of  $\Delta\Pi_1 = 75.2$  seconds. However, dynamical processes taking place inside the star can affect the frequency of the modes. In particular, wave propagation at low frequencies is affected by rotation and magnetism (e.g., Ouazzani et al. 2013; Fuller et al. 2015). In the following, we use  $\tau_{\text{obs}}$  to denote the stretched period computed from observed oscillation frequencies:

$$\Delta\tau_{\text{obs}_m} = \int_{\nu_{\text{obs}_{m,n+1}}}^{\nu_{\text{obs}_{m,n}}} d\tau_{\text{obs}} = \int_{\nu_{\text{obs}_{m,n+1}}}^{\nu_{\text{obs}_{m,n}}} -\frac{1}{\zeta} \frac{d\nu_{\text{obs}}}{\nu_{\text{obs}}^2}. \quad (15)$$

If mixed-mode frequencies are not affected by any external perturbations, then  $\nu_{\text{obs}} = \nu$ ,  $d\tau_{\text{obs}} = d\pi$ , and Eq. 15 is reduced to Eq. 11. However, ( $\ell = 1, m$ ) mixed modes might be spaced differently depending on dynamical mechanisms taking place inside the star. We therefore introduced  $\Delta\tau_{\text{obs}_m}$  in Eq. 15, which stands for the observed period spacing associated with modes with ( $\ell = 1, m$ ) components in a star (see Gehan et al. 2018).

One of the dynamical mechanisms known to produce different spacings between different "m" orders is rotation. Rotation lifts the degeneracy among the frequencies of modes with the same ( $n, \ell$ ) but different azimuthal orders,  $m$  (Gizon & Solanki 2003; García & Ballot 2019). Rotation effects on mixed mode frequencies can be approximated on the first order as evolved stars with solar-like oscillations are relatively slow rotators (in contrast to the case of g-modes in rapidly rotating dwarfs, see Aerts 2021). We define  $\delta\nu_{\text{rot}}$  as the frequency perturbation induced by rotation, so that the observed frequencies are expressed as a function of the azimuthal order,  $m$ :

$$\nu_{\text{obs}_m} = \nu_{m=0} + m\delta\nu_{\text{rot}}. \quad (16)$$

For mixed modes that are sensitive to the rotation rate of both the envelope and the core, we approximate  $\delta\nu_{\text{rot}}$  as (Goupil et al. 2013):

$$\delta\nu_{\text{rot}} = \zeta\delta\nu_{\text{rot},g} + (1 - \zeta)\delta\nu_{\text{rot},p}. \quad (17)$$

This approximation has proven to be sufficient to probe spatially-resolved rotation profiles in stellar interiors (e.g., Deheuvels et al. 2014; Di Mauro et al. 2016; Triana et al. 2017). In addition, g- $m$  modes are mostly sensitive to the rotation rate near the core, so that the rotational splitting associated with the internal process can be approximated as:

$$\delta\nu_{\text{rot}} \approx \zeta\delta\nu_{\text{rot},g}. \quad (18)$$

The observed g- $m$  mode frequencies in the PSD in the presence of rotation therefore depends on the azimuthal order  $m$  as:

$$\nu_{\text{obs}_m} = \nu + \delta\nu_{\text{rot}_m}, \quad (19)$$

with  $\nu = \nu_{m=0}$  the unperturbed mixed-mode frequency and  $\delta\nu_{\text{rot}_m} = m\zeta\delta\nu_{\text{rot},g}$ . As a result of Eq. 19, one ( $n, \ell$ ) mode is split into three evenly spaced components resulting from

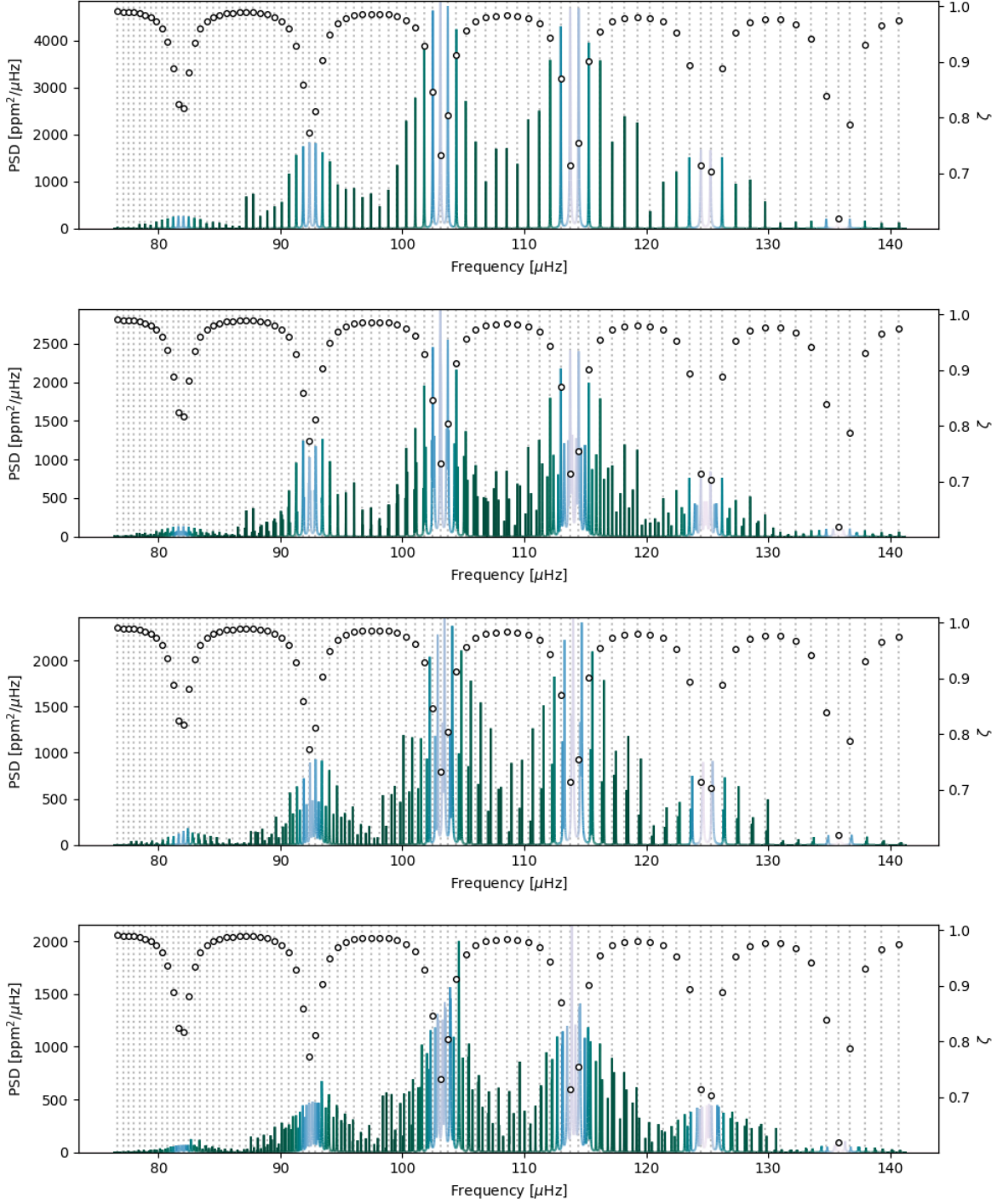


**Fig. 1.** PSDs comprised of mixed dipolar oscillation modes of a simulated RGB star with  $\nu_{\max} = 110 \mu\text{Hz}$  and  $\Delta\Pi_1 = 75.2$  sec. *Top panel:* Non-rotating, non-magnetized model. *Second panel:* Model rotating with  $\delta\nu_{\text{rot}} = 0.69 \mu\text{Hz}$ ,  $i = 45^\circ$ . *Third panel:* Model magnetized with  $\delta\nu_{\text{mag}}(\nu_{\max}) = 50\delta f_{\text{res}} = 0.4 \mu\text{Hz}$ ,  $i = 45^\circ$ . *Bottom panel:* Model rotating and magnetized with  $\delta\nu_{\text{rot}} = 0.69 \mu\text{Hz}$ ,  $\delta\nu_{\text{mag}}(\nu_{\max}) = 0.4 \mu\text{Hz}$ ,  $i = 45^\circ$ . The  $\zeta$  function is overplotted on each panel to indicate the location of p-*m* modes (dips) and g-*m* modes (maxima), while the color of the PSD varies according to the zeta function value for better visualization of the nature of the modes (dark green: g-*m* dipolar modes, light blue: p-*m* dipolar modes). Dotted vertical lines indicate the location of the modes for the non-rotating, non-magnetized model.

the first-order effect of rotation on oscillation frequencies. A first-order rotating synthetic spectrum with a rotation splitting  $\delta\nu_{\text{rot,g}} = 0.69 \mu\text{Hz}$  is represented on the second panel of Fig. 1.

By assuming that the rotational perturbation of g-*m* modes is independent of the mixed-mode frequencies at first order (i.e. we neglect the frequency dependency of the  $\zeta$  function close to g-*m*

modes,  $\zeta(\nu) \approx \zeta$ ), we have  $d\nu_{\text{obs}_m} \approx d\nu$ . By using Eq. 11, Eq. 15 can be rewritten as a function of the unperturbed  $d\tau$  as:

$$\Delta\tau_{\text{obs}_m} = \int \frac{d\tau}{\left(1 + \frac{\delta\nu_{\text{rot,g}}}{\nu}\right)^2}. \quad (20)$$

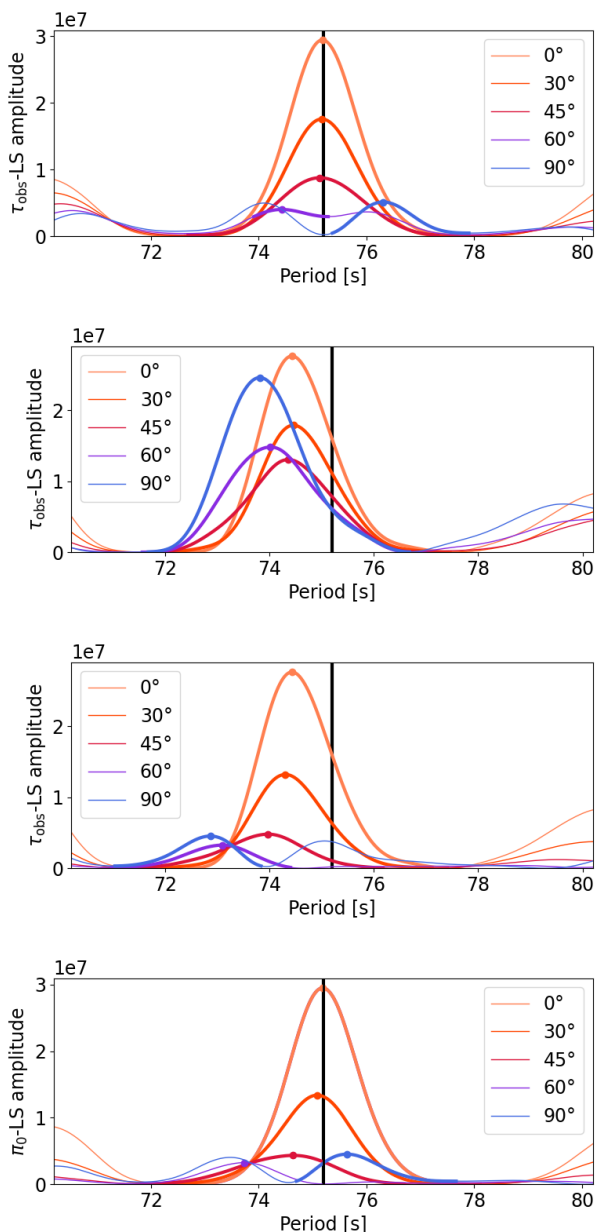


**Fig. 2.** LS periodograms for different stellar models. *Top panel:*  $d\tau_{\text{obs}}$ -LS periodogram for a simulated star rotating such as  $\delta v_{\text{rot},g} = 0.69 \mu\text{Hz}$ . *Second panel:* Same diagram for a simulated magnetized, non-rotating star such as  $\delta v_{\text{mag},g}(v_{\text{max}}) = 0.4 \mu\text{Hz}$ . *Third panel:* Same diagram for a simulated magnetized and rotating star such as  $\delta v_{\text{rot},g} = 0.69 \mu\text{Hz}$  and  $\delta v_{\text{mag},g}(v_{\text{max}}) = 0.4 \mu\text{Hz}$ . *Bottom panel:*  $d\tau_0$ -LS periodogram of the same rotating and magnetized star. In each panel, the star is observed with various inclination angles with respect to the rotation axis of the star following the color code in the legend. LS periodogram are zoomed around the true value of the period spacing  $\Delta\Pi_1 = 75.2$  sec.

As a result, the period spacing of pure g-modes defined from Eq. 12 can be measured from the distance between  $m = 0$  modes with consecutive radial order  $n$  expressed in the stretch variable  $\tau_{\text{obs}}$  even in the rotating case. The LS method described in Section 2.1.4 can thus still be computed from the stretched PSD (Eq. 15) in the rotating case to retrieve  $\Delta\Pi_1$ , because  $m = 0$  modes will maintain the signal of unperturbed g- $m$  mixed-modes in the LS periodogram.

Previous studies (Vrard et al. 2016; Gehan et al. 2018) therefore neglected the effect of rotation on the measurement of  $\Delta\Pi_1$ . Indeed, as long as the  $m = 0$  component (that is not affected by rotation) is visible in the PSD, the methodology (described in Sect. 2.1.4) is still valid and the effect of rotation on the measured  $\Delta\Pi_1$  can be neglected (we refer the reader to Vrard et al. 2016, for more details about the effect of rotation on  $\Delta\Pi_1$  measurement when the star is not observed pole-on). However, if the star is observed edge-on (inclination angle close to  $90^\circ$ ), the non-perturbed frequency of mixed modes (associated with  $m = 0$  modes) is no longer present in the PSD. As a result, for stars observed with high inclination ( $i \geq 45^\circ$ ) the stretching of the PSD according to Eq. 15 may not reveal the periodicity of mixed modes from the data.

Such a phenomenon is represented on the top panel of Fig. 2. It shows the LS periodogram computed for a typical RGB star, with a rotation signature, ( $\delta v_{\text{rot}} = 0.69 \mu\text{Hz}$ ), and observed with various stellar inclinations ( $i$ ). We show that for  $i \lesssim 45^\circ$ , the measurement of  $\Delta\Pi_1$  is not affected by rotation as only the amplitude (not the period) of the main detected peak is altered. However, for larger inclination angles, the impact of the  $m = -1, 1$  components dominate the LS periodogram. As demonstrated by the dependency in  $(1 + \frac{\delta v_{\text{rot},m}}{v})^{-2}$  in Eq. 20, the  $m = 1$  (and  $= -1$ ) periods are not evenly spaced in the commonly used  $d\tau_{\text{obs}0}$ -stretched spectrum, leading to a spreading of the power density around non-resolved  $m = 1$  and  $m = -1$  peaks in the LS periodogram around  $\Delta\Pi_1$ .

As presented in Section 2.1.4, the  $\delta(\Delta\Pi_{1,\text{over}})$  precision obtained on  $\Delta\Pi_1$  strongly depends on the amplitude of the peak in the LS periodogram. When the amplitude goes to zero in the LS periodogram as the inclination increases towards  $|i| \approx 90^\circ$ , the uncertainty on the measurement of  $\Delta\Pi_1$  goes to infinity. We conclude that the measurement of  $\Delta\Pi_1$  with this LS method is robust only for rotating stars with relatively low inclination angles ( $i \leq 45^\circ$ ).

### 3. Effect of internal magnetism on the measurement of g-mode period spacing

#### 3.1. Magnetic field topology and amplitude inside evolved stars with solar-like oscillations

Evolved stars with solar-like oscillations that are considered in this work are descendants of low- and intermediate-mass main sequence stars, which have themselves evolved from fully convective bodies during the PMS. Convective zones are known to generate and to host stochastic dynamo fields (Brun & Browning 2017). Over the past 20 years, many studies have investigated how such dynamo-generated fields might remain trapped into the radiative interior once the convection has come to an end inside the star during the MS (e.g., Braithwaite & Spruit 2004; Braithwaite & Nordlund 2006; Braithwaite 2008; Arlt & Weiss 2014; Emeriau-Viard & Brun 2017). Braithwaite & Spruit (2004) were the first to simulate the relaxation of completely stochastic fields in a non-rotating radiative interior. They show that dynamo-generated fields can become stabilized when the convection process ends. From these simulations, we deduce that initial stochastic dynamo fields placed into a stably stratified interior might relax into stable, large-scale, mixed poloidal and toroidal magnetic field configurations (Braithwaite 2008). This inverse turbulent cascade mechanism is described theoretically in Duez & Mathis (2010). Purely toroidal and



purely poloidal magnetic configurations are known to be unstable (e.g., Tayler 1973; Markey & Tayler 1973; Braithwaite 2006, 2007). Combining toroidal and poloidal components ensures the stability of the field (Tayler 1980; Braithwaite 2009). Once a stable field is formed in the radiative interior, the characteristic Ohmic timescale on which the field gets dissipated is of about  $10^{10}$  years, much longer than the lifetime of the star. Hence, if stable magnetic fields are formed inside the radiative interior during the main sequence, they would remain trapped inside the radiative interior on the RGB if no external dissipating mechanisms are at work.

**Field topology:** The topology and energy of stable mixed poloidal and toroidal field has been investigated numerically by Braithwaite (2008), and semi-analytically by Akgün et al. (2013). Duez & Mathis (2010) provided a semi-analytic description of the stable mixed toroidal and poloidal fields similar to those resulting from the simulations of Braithwaite (2008):

$$\mathbf{B}(r, \theta) = \frac{1}{r \sin \theta} \left( \nabla \psi(r, \theta) \wedge \mathbf{e}_\varphi + \lambda \frac{\psi(r, \theta)}{R} \mathbf{e}_\varphi \right), \quad (21)$$

where  $\psi$  is the stream function satisfying

$$\psi(r, \theta) = \mu_0 \alpha \lambda \frac{A(r)}{R} \sin^2 \theta, \quad (22)$$

with  $\mu_0$  as the vacuum magnetic permeability,  $\alpha$  as a normalization constant fixed by the chosen magnetic-field amplitude,  $\lambda$  as the eigenvalue of the problem to be determined,  $R$  as the radius of the star, and

$$A(r) = -r j_1 \left( \lambda \frac{r}{R} \right) \int_r^R y_1 \left( \lambda \frac{x}{R} \right) \rho x^3 dx - r y_1 \left( \lambda \frac{r}{R} \right) \int_0^r j_1 \left( \lambda \frac{x}{R} \right) \rho x^3 dx, \quad (23)$$

with  $j_1$  ( $y_1$ ) as the first-order spherical Bessel function of the first (second) kind (Abramowitz & Stegun 1972) and  $\rho = \rho(r)$  the hydrostatic density profile of the star. To confine the field inside the radiative interior, we set  $\lambda$  as the smallest positive value for  $\mathbf{B}$  to vanish at the convective-radiative boundary. The resulting magnetic field configuration for a typical RG ( $M = 1.5 M_\odot$ ,  $Z = 0.02$ , 2.71 Gyr) is represented in Fig. 3.

**Field amplitude:** We cannot (thus far) detect buried magnetic fields through direct observations and so, we can only try to predict their amplitude. Considering the fossil field scenario described above, and assuming that the magnetic flux is conserved inside the mass coordinate of the radiative interior as the star evolves from the MS, Bugnet et al. (2021) showed that the magnetic field amplitude inside red giants should be in the range  $[10^5 : 10^7]$  Gauss (depending on the efficiency of the dynamo action, see Augustson et al. 2019). We refer to Bugnet et al. (2021) for details about the conservation of the magnetic flux along the evolutionary process resulting in these numbers.

### 3.2. Magnetic effect on mixed-mode frequencies

The effect of stable fossil internal magnetic fields on the frequencies of solar-like mixed oscillations has been investigated by Bugnet et al. (2021), Mathis et al. (2021), and Loi (2021). By performing a first-order perturbative analysis on the eigenfrequencies of the modes, Bugnet et al. (2021) showed that axisymmetric fossil magnetic fields lifts the degeneracy on the

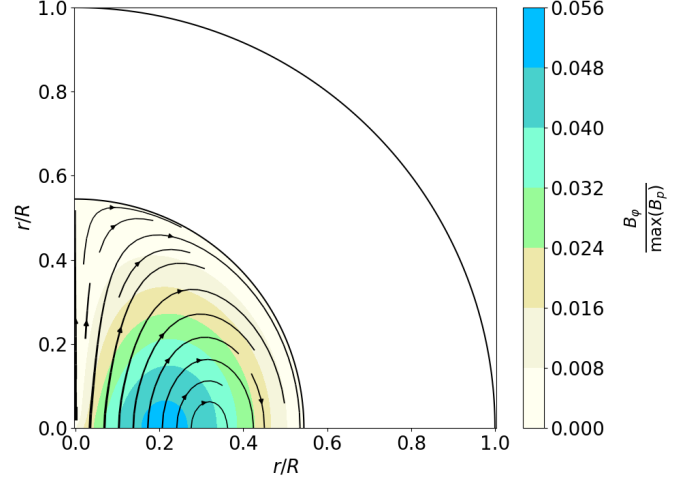


**Fig. 3.** Magnetic field configuration inside a  $M = 1.5 M_\odot$ ,  $Z = 0.02$ , 2.71 Gyr evolved star with solar-like oscillations on the RGB. The field is confined within the inner black line (convective-radiative boundary) and the stellar surface is indicated by the outer black line.

azimuthal order of mixed modes and generates an asymmetric shift in the observed frequencies. The authors derived the complete first-order perturbation and demonstrated, through the use of the pulsation code GYRE (Townsend & Teitler 2013), that such magnetic signature on the mixed-mode frequency pattern might be detectable in the *Kepler* data. Mathis et al. (2021) derived asymptotic expressions for the magnetic signature on mixed-mode frequencies corresponding to the dominant effect revealed by Bugnet et al. (2021). Finally, Mathis et al. (2021) study showed that the effect of a mixed poloidal and toroidal field aligned with the rotation axis of the star (as represented in Fig. 3) on  $g$ - $m$  mixed-mode frequencies can be approximated by

$$\delta \nu_{\text{mag}, g_m}(\nu) = \frac{1}{2(2\pi)^4} \frac{B_0^2}{4\pi\rho_c R_{\text{rad}}^2 \nu} \frac{N_{\text{max}}^2}{\nu^2} \ell(\ell+1) C_{\ell, m}(\nu) \times \frac{\int_0^1 \frac{b_r^2 \widehat{N}^2}{(\rho/\rho_c) x^2} \widehat{N} \frac{dx}{x}}{\int_0^1 \widehat{N} \frac{dx}{x}}, \quad (24)$$

where we introduce: **1.** the dimensionless radius  $x = r/R_{\text{rad}}$  inside the radiative interior, with  $R_{\text{rad}}$  the radius of the radiative zone, **2.** the ratio of the dimensionless density profile  $\rho$  inside the radiative interior and of the central density,  $\rho_c$ , **3.** the maximum of the Brunt-Väisälä frequency,  $N_{\text{max}}$ , and its dimensionless radial profile,  $\widehat{N} = N(r)/N_{\text{max}}$ , and **4.** the magnetic field amplitude along the field lines,  $B_0$ , and its dimensionless radial profile,  $b_r$  and the angular integral:

$$C_{\ell, m} = \frac{\int_0^\pi \left[ \left| \cos \theta \partial_\theta Y_\ell^m \right|^2 + m^2 \left| \frac{\cos \theta}{\sin \theta} Y_\ell^m \right|^2 \right] \sin \theta d\theta}{\ell(\ell+1)}. \quad (25)$$

This prescription of the magnetic signature on dipolar mixed-mode frequencies is key for a search for internal magnetic fields inside the radiative interior of evolved stars.

From Eq. 24, we deduce the expression of the internal magnetic perturbation on mixed-mode frequencies for each of the  $m$  azimuthal degree as:

$$\delta v_{\text{mag}_m}(\nu) = m^* \zeta \delta v_{\text{mag}_g}(\nu) = m^* \zeta \frac{A B_0^2}{\nu^3}, \quad (26)$$

with  $m^* = \frac{|m|+1}{2}$ ,  $A$  as the normalization factor depending on the magnetic field topology and of the structure of the star containing all remaining terms in Eq. 24 (see Mathis et al. 2021, for more details),  $B_0$  as the magnetic field amplitude, and  $\delta v_{\text{mag}_g}$  as the magnetic effect associated with pure g-modes. As a result, the magnetic perturbation is a function of the frequency, and the perturbation on the  $m = 1$  and  $m = -1$  mixed-mode components are equal to twice the perturbation on the  $m = 0$  component. The magnetic signature is therefore very different from the rotational signature, as all the  $m$  components are affected and form a non-symmetric pattern in frequency (see Bugnet et al. 2021).

### 3.3. Error of the measurement of $\Delta\Pi_1$ in the presence of magnetic fields

We now consider a non-rotating star and an internal axisymmetric magnetic field to investigate its effect on the LS methodology to estimate  $\Delta\Pi_1$ . In the presence of magnetism, the observed ( $n, \ell = 1, m$ ) frequencies write as the following function of the unperturbed mixed-mode frequency:

$$\nu_{\text{obs}_m} = \nu + \delta v_{\text{mag}_m}(\nu), \quad (27)$$

so that

$$\frac{d\nu_{\text{obs}_m}}{d\nu} = 1 - 3 \frac{\delta v_{\text{mag}_m}(\nu)}{\nu}. \quad (28)$$

In the case of magnetism only, we obtain an equation analog to Eq. 20:

$$\Delta\tau_{\text{obs}_m} \approx \Delta\Pi_1 \frac{1 - 3 \frac{\delta v_{\text{mag}_m}(\nu)}{\nu}}{\left(1 + \frac{\delta v_{\text{mag}_m}(\nu)}{\nu}\right)^2}. \quad (29)$$

As  $\Delta\tau_{\text{obs}_m} \neq \Delta\Pi_1$  for all  $m \in [-1, 0, 1]$  values through Eq. 29, the classical stretching made by using Eq. 15 should not result in an accurate measurement of  $\Delta\Pi_1$  for any of the  $m$  orders, as opposed to the rotational case where the  $m = 0$  modes remain evenly spaced. Equation 29 therefore demonstrates that the use of the  $d\tau_{\text{obs}}$  period stretching (see Eq. 15), as developed by Vrad et al. (2016), leads to biased estimates of  $\Delta\Pi_1$  if the radiative interior of the star is magnetized, because  $d\tau_{\text{obs}} = d\tau_{\text{obs}_0} \neq d\pi$ .

In the third panel of Fig. 1 we represent the PSD of a magnetized star with  $\delta v_{\text{mag}}(\nu_{\text{max}}) = 50\delta f_{\text{res}}$ , considering an inclination angle of  $i = 45^\circ$ . The  $d\tau_{\text{obs}}$ -LS periodogram of such a PSD is represented in the second panel of Fig. 2 following Eq. 15, along with other LS periodogram computed from artificial data corresponding to various observation angles. As expected, stretching the PSD following Eq. 15 does not allow for an accurate measurement of  $\Delta\Pi_1$  when the star is magnetized. The erroneous estimation of  $\Delta\Pi_1$  increases with the inclination angle, as  $m = 1$  and  $m = -1$  modes, which are the most affected by magnetic fields, tend to dominate the spectrum when  $i$  increases. To correct the measurement of  $\Delta\Pi_1$ , we adapt the stretch function to account for the true period of g-mode  $\pi$ , instead of  $\tau_{\text{obs}}$ :

From Eq. 29 we deduce that the  $\pi$  function can be written as a function of one of the  $m = 1, m = 0$ , or  $m = -1$  mode frequencies, following:

$$d\pi = -\frac{1}{\zeta} \frac{d\nu_{\text{obs}_m}}{\nu^2} \frac{\left(1 + \frac{\delta v_{\text{mag}_m}(\nu)}{\nu}\right)^2}{1 - 3 \frac{\delta v_{\text{mag}_m}(\nu)}{\nu}}. \quad (30)$$

### 3.4. Combined effects of rotation and magnetism on the measurement of $\Delta\Pi_1$

The artificial PSD of a RG in the presence of rotation ( $\delta v_{\text{rot}_g} = 0.69 \mu\text{Hz}$ ) and an internal stable magnetic field ( $\delta v_{\text{mag}_g}(\nu_{\text{max}}) = 0.4 \mu\text{Hz}$ ) observed from an angle  $i = 45^\circ$  is represented in the bottom panel of Fig. 1 for reference. As the star is magnetized, the use of Eq. 15 does not lead to an accurate value of  $\Delta\Pi_1$  with the  $d\tau_{\text{obs}}$ -LS method, as represented in the third panel of Fig. 2 for various inclination angles. In the presence of both magnetism and rotation, observed frequencies rewrite at first order as:

$$\nu_{\text{obs}_m} = \nu + \delta v_{\text{mag}_m}(\nu) + \delta v_{\text{rot}_m}, \quad (31)$$

and  $\frac{d\nu_{\text{obs}_m}}{d\nu}$  still follows Eq. 28. Therefore, the relation between the period  $\pi$  adequate to measure the period spacing,  $\Delta\Pi_1$ , and the observed period of modes with the same  $m$  azimuthal order  $\tau_{\text{obs}_m}$  is:

$$d\pi = -\frac{1}{\zeta} \frac{d\nu_{\text{obs}_m}}{\nu^2} \frac{\left(1 + \frac{\delta v_{\text{mag}_m}(\nu)}{\nu} + \frac{\delta v_{\text{rot}_m}}{\nu}\right)^2}{1 - 3 \frac{\delta v_{\text{mag}_m}(\nu)}{\nu}}. \quad (32)$$

## 4. Ways to probe the presence of internal magnetism from the measurement of $\Delta\Pi_1$

### 4.1. The $d\pi_0$ -LS method for measuring $\Delta\Pi_1$ from axisymmetric mixed modes

Equations 30 and 32 can both be rewritten, independently of the presence of rotation, as:

$$d\pi = -\frac{1}{\zeta} \frac{d\nu_{\text{obs}_m}}{\nu^2} \frac{1}{1 - 3 \frac{\delta v_{\text{mag}_m}(\nu)}{\nu}}. \quad (33)$$

The measurement of  $\Delta\Pi_1$  therefore depends on the magnetic field amplitude, on the inner structure of the stars through the dependency on  $A$ , and on the unperturbed frequency of mixed modes. To retrieve  $\Delta\Pi_1$  from the integration of Eq. 33, only modes with a shared  $m$  order must be considered simultaneously. As the  $m = 1$  and  $m = -1$  components cannot be independently observed for stochastically-excited solar-like oscillations (Gizon & Solanki 2003), it is convenient to focus on  $m = 0$  modes.

Using Eq. 27 (for the magnetized, non-rotating case) or Eq. 31 (for the magnetized, rotating case) for  $m = 0$  mixed modes, the equation describing the unperturbed frequencies of the modes is:

$$\nu^4 - \nu_{\text{obs}_0} \nu^3 + \frac{\zeta A B_0^2}{2} = 0. \quad (34)$$



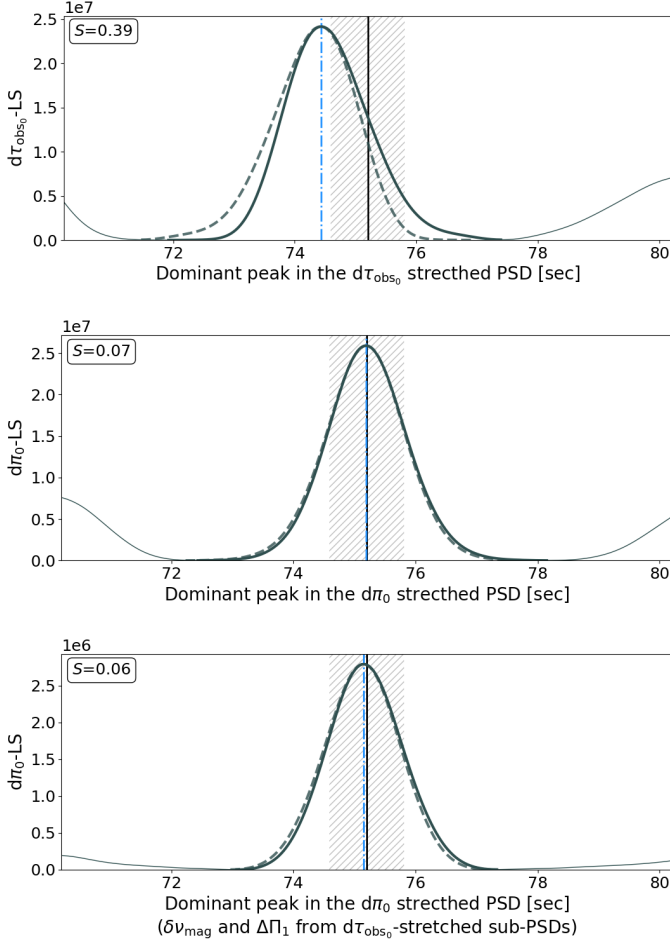


**Fig. 4.** LS periodograms for simulated stars. *Top panel:* LS periodogram of the  $d\tau_{\text{obs}}$ -stretched PSD for a simulated magnetized RG observed pole-on. *Middle panel:*  $d\pi_0$ -LS periodogram for the simulated magnetized RG, using  $\Delta\Pi_1 = 75.2$  sec and  $\delta\nu_{\text{mag}}(\nu_{\text{max}}) = 0.40 \mu\text{Hz}$ . *Bottom panel:* LS periodogram of the  $d\pi_0$ -stretched PSD for the simulated magnetized RG by using  $\Delta\Pi_1 = 75.13$  sec and  $\delta\nu_{\text{mag}}(\nu_{\text{max}}) = 0.38 \mu\text{Hz}$  (as calculated in Sect. 4.5). In each panel, the black line indicates the true value of  $\Delta\Pi_1$ , and the dot-dashed blue line indicates the period associated with the maximum amplitude in the LS periodogram. Dashed grey curves are the mirrored central peak around the period associated with the maximum amplitude in the LS periodogram. Curves are thicker within the central peak for better visualization. Hatched areas indicate the typical uncertainty  $\delta(\Delta\Pi_1)_{\text{res}} = 0.6$  seconds on the measurement of  $\Delta\Pi_1$  from LS-based methods according to the study of Vrard et al. (2016), centered around  $\Delta\Pi_1 = 75.2$  sec. The skewness of the dominant peak calculated with Eq. C.1 is indicated in the top left corner of each panel.

As we focus on  $m = 0$  modes, rotation does not play a role (for the slow rotation rates of red giants). Equation 34 can be solved analytically to obtain  $\nu = f_0(\nu_{\text{obs}})$ , following Appendix B. The measurement of  $\Delta\Pi_1$  in the presence of internal magnetism therefore strongly depends on our ability to detect magnetically shifted  $m = 0$  dipolar modes in the PSD.

To demonstrate the efficiency of the corrected  $\pi$  stretching defined by Eq. 33, we stretch the PSD of a simulated magnetized star observed pole-on ( $i = 0^\circ$ ) according to the  $m = 0$  mag-

netized stretch period  $\pi_0$  defined as a function of the observed PSD:

$$d\pi_0 = -\frac{1}{\zeta} \frac{d\nu_{\text{obs}}}{f_0(\nu_{\text{obs}})^2} \frac{1}{1 - \frac{3\zeta}{2} \frac{AB_0^2}{f_0(\nu_{\text{obs}})^4}}. \quad (35)$$

The top panel of Fig. 4 shows the LS periodogram of the  $d\tau_{\text{obs}}$ -stretched PSD of a star seen pole-on (only  $m = 0$  components are visible in the PSD), with an axisymmetric magnetic field perturbing mixed-mode frequencies inside the radiative interior following Eq. 27. The amplitude of the field is taken such as the magnetic perturbation at  $\nu_{\text{max}}$  (given by  $AB_0^2/\nu_{\text{max}}^3$ ) is equal to 50 times the frequency resolution,  $\delta f_{\text{res}}$ , in the PSD. As  $\delta f_{\text{res}} \approx 0.008 \mu\text{Hz}$  for the four-year observations during the *Kepler* mission, the magnetic signature at  $\nu_{\text{max}}$  is chosen to be  $0.4 \mu\text{Hz}$ . We observe that the measured period spacing (dotted-dashed blue line) is smaller than the true g-mode period spacing (black line), with an offset of about 1% (as already discussed in Sect. 3.3). We conclude that if we do not have any prior on the magnetic field amplitude inside the observed star, then we do not have any dependable way of obtaining an accurate value for  $\Delta\Pi_1$ .

For the middle panel of Fig. 4, we assume that we know the value of  $\delta\nu_{\text{mag}}$ . We can then represent the LS periodogram of the  $d\pi_0$ -stretched PSD ( $d\pi_0$ -LS periodogram) of the simulated magnetized RG according to Eq. 35. We display a measurement of the period associated with the maximum power in the PSD (red dashed line) at  $\Delta\Pi_{\text{LS}} = 75.19$  sec. The true period spacing used to simulate the star being  $\Delta\Pi_1 = 75.20$  sec, it corresponds to an estimation error of the  $\Delta\Pi_1$  parameter of about 0.01% in the presence of magnetism through the use of  $m = 0$  modes alone. In Appendix D, we provide the analogous results when considering  $m = \pm 1$  oscillation modes, which leads to a more complicated analysis in the case of rotation stars as  $m = \pm 1$  are excited with the same amplitude (Gizon & Solanki 2003) and one cannot exist without the other.

#### 4.2. Effect of the inclination of the star on the accuracy of $\Delta\Pi_1$ with the $d\pi_0$ -LS method

The measurement of  $\Delta\Pi_1$  with this " $d\pi_0$ -LS" method is robust only for stars with relatively low inclination angles, as the amplitude of the  $m = 0$  modes must emerge above the noise level in the PSD. In the bottom panel of Fig. 2 we represent the  $d\pi_0$ -LS periodogram of the simulated rotating and magnetized model (see the corresponding PSD in the bottom panel of Fig. 1) observed with various inclination angles. When the star is observed pole-on, the  $d\pi_0$ -stretching leads to a nearly perfect estimate of  $\Delta\Pi_1$ . As the inclination increases and the amplitude of the  $m = \pm 1$  components increase with respect to the  $m = 0$  component's amplitude, the  $d\pi_0$ -stretching is not adapted to the data anymore, and the measurement of the period spacing becomes biased again. For the rest of this study, we set our focus on stars with  $i \leq 30^\circ$  to ensure that  $\Delta\Pi_1$  is accurately estimated from the period associated with the maximum of the  $d\pi_0$ -LS periodogram even when the star is rotating.

### 4.3. Skewness of the dominant peak in the $d\tau_{\text{obs}_0}$ -LS periodogram as a signature of internal magnetism

On each panel of Fig. 4 we mirror the dominant peak in the LS periodogram around the measured period spacing and represent it by the dashed grey curves. This visual trick allows to unveil the asymmetry of the dominant peak in the  $d\tau_{\text{obs}}$ -stretched LS periodogram (first panel), caused by the dependency in frequency of the magnetic effect.

Current interpretations of the oscillation spectra have ignored to search for skewness in the LS periodogram maxima. We prove here that non-zero skewness can be used as a detection method for internal magnetism (see Appendix C for more details). Examining RGB stars more closely could reveal these small magnetic signatures. However, other physical processes such as non-uniform rotation could lead to skewed distribution in the LS periodogram. Therefore, the skewness method should be used with care. In the following sections, we develop the main detection method for internal magnetic fields.

### 4.4. Local measurement of $\Delta\Pi_1$ in the PSD as a probe for internal magnetic fields

We dig further into the ability to detect the presence of internal magnetism from LS-based measurements of  $\Delta\Pi_1$ , and develop a method to get a first estimate of the magnetic field amplitude without needing the very challenging fit of Eq. 24 to the PSD. The effect of an axisymmetric mixed poloidal and toroidal field buried in the radiative interior of RGB stars generates a characteristic signature on the different azimuthal  $m$  components. All  $g$ - $m$  dipolar frequencies described by Eq. 27 (see Bugnet et al. 2021; Mathis et al. 2021) are shifted towards higher frequencies following the scaling law given by Eq. 26. The shift of  $m = \pm 1$  modes is twice the shift of  $m = 0$  modes as represented in the third panel of Fig. 1, but they all vary with the unperturbed frequency of the mode as  $1/\nu^3$ . The magnetic signature is thus much higher at lower frequencies in the PSD. The dependency of the magnetic shift with the mode frequency lies at the basis of the bias in the measurement of  $\Delta\Pi_1$ , shown in Fig. 4. In addition, the  $1/\nu^3$  dependency changes the observed value  $\Delta\tau_{\text{obs}}$  along the observational frequency range considered here ( $\nu \in [\nu_{\text{max}} - 3\Delta\nu : \nu_{\text{max}} + 3\Delta\nu]$ ). We therefore investigate how local measurements of  $\Delta\tau_{\text{obs}}$  for various frequency ranges might allow to detect the presence of buried magnetic fields.

To do so, we create subsamples of the simulated model's  $d\tau_{\text{obs}}$ -stretched PSD on  $(2\Delta\nu)$ -wide intervals around each of the  $\nu_{p_n}$  modes as represented in the left panels of Fig. 5. We compute the  $d\tau_{\text{obs}}$ -LS periodogram for each sub-PSD (see middle panels of in Fig. 5) and we measure the period associated with their maximum power. In the right panel, we indicate these  $\Delta\tau_{\text{obs}_n}$  values as a function of  $\nu_{p_n}$ . The row a) in Fig. 5 represents a non-magnetized star observed pole-on. None of the  $m = 0$  visible modes are affected by any internal processes, therefore, all the measurements of  $\Delta\tau_{\text{obs}_n}$  are consistent with the value of  $\Delta\Pi_1$  as represented in the top right panel. The b) star is magnetized with  $\delta\nu_{\text{mag},g}(\nu_{\text{max}}) = 0.4 \mu\text{Hz}$ , and observed pole-on. As expected from the  $1/\nu^3$  dependency of the frequency shift, the period spacing  $\Delta\tau_{\text{obs}_n}$  measured from the  $d\tau_{\text{obs}}$ -LS periodogram increases and gets closer to the known  $\Delta\Pi_1$  value as the  $\nu_{p_n}$  frequency increases (see bottom-right panel).

When using Eq. 13 to account for measurement errors from the LS method as done by Vrad et al. (2016), uncertainties on all  $\Delta\tau_{\text{obs}_n}$  measurements should be equal. However, the

signal-to-noise ratio (S/N) decreases from  $\nu_{\text{max}}$  towards the edges of the  $[\nu_{\text{max}} - 3\Delta\nu : \nu_{\text{max}} + 3\Delta\nu]$  interval. The measurement of the periodicity in the stretched spectrum should therefore take into account that the white noise in the PSD will not pollute the signal on every interval in the same way. The impact of the amplitude of the signal in the stretched PSD on the amplitude in the LS periodogram is visualized in middle panels of Fig. 5. We therefore use the oversampling resolution from Eq. 14, which is anti-correlated to the peak amplitude. The measurement of the oversampling uncertainty requires a normalization to the noise level in the LS periodogram. Here, we chose not to include any noise in our artificial spectra as the distribution and amplitude of noise might vary a lot in real observations. By drawing a few pure  $\chi^2_2$  white noise PSDs and performing their LS periodogram, we estimate the typical contribution of the photon noise corresponding to a high S/N in the PSD and normalize the result. We then obtain a normalized LS periodogram as represented in Fig. 5, with the normalized amplitude of the highest peak of a few dozens, representative of a real RGB asteroseismic data (as discussed in Vrad et al. 2016). The orange peak corresponding to a frequency range in the PSD with modes of very small amplitude have an amplitude in the LS periodogram considered too low with respect to the noise level (i.e.,  $A < 13$ , Vrad et al. 2016) for the detection to be precise, which explains the large uncertainty reported in the right panels when measuring  $\Delta\tau_{\text{obs}_n}$  at low frequency.

We consider this  $\delta(\Delta\Pi_{\text{over}})$  uncertainty as the smallest possible uncertainty. Indeed, very small uncertainties can be reached only when the gravity offset  $\epsilon_g$ , intervening in the pure  $g$ -mode pattern, is perfectly known. As this is not strictly the case in real data, we also perform the following study by taking into account the resolution uncertainty defined by Eq. 13.

### 4.5. Estimation of the magnetic splitting from $d\tau_{\text{obs}_0}$ -stretched PSD subsamples

We use the trend in the  $\Delta\tau_{\text{obs}_n} - \nu_{p_n}$  diagram to correct the  $\Delta\Pi_1$  measurement for magnetized stars observed pole-on and to constrain the value of the magnetic splitting. Cutting the spectra into smaller frequency intervals allows to approximate Eq. 30. By considering  $\nu \approx \nu_{p_n}$  on each small frequency intervals:

$$\Delta\tau_{\text{obs}_n} \approx C(\nu_{p_n}, \delta\nu_{\text{mag},g}) \times \Delta\Pi_1, \quad (36)$$

with

$$C(\nu_{p_n}, \delta\nu_{\text{mag},g}) = \frac{1 - \frac{3}{2}\zeta_g(\nu_{p_n})\frac{\delta\nu_{\text{mag},g}}{\nu_{p_n}}}{\left(1 + \frac{1}{2}\zeta_g(\nu_{p_n})\frac{\delta\nu_{\text{mag},g}}{\nu_{p_n}}\right)^2}. \quad (37)$$

With this approximation, we consciously underestimate the effect of the magnetic field on the frequencies of the modes and we therefore underestimate the value of  $\Delta\Pi_1$ . However, this loss of accuracy is counterbalanced by the possibility of performing a simple fit of the  $(\Delta\Pi_1, \delta\nu_{\text{mag},g})$  parameters from the  $\Delta\tau_{\text{obs}_n} - \nu_{p_n}$  data represented of the right panels. We thus fit the value of the magnetic parameter  $\delta\nu_{\text{mag},g}$  along with  $\Delta\Pi_1$  to adjust the following function derived from Eq. 36 in the  $\Delta\tau_{\text{obs}_n} - \nu_{p_n}$  diagram:

$$\mathcal{F}(\Delta\Pi_1, \delta\nu_{\text{mag},g}) : \nu_{p_n} \rightarrow C(\nu_{p_n}, \delta\nu_{\text{mag},g}) \times \Delta\Pi_1. \quad (38)$$

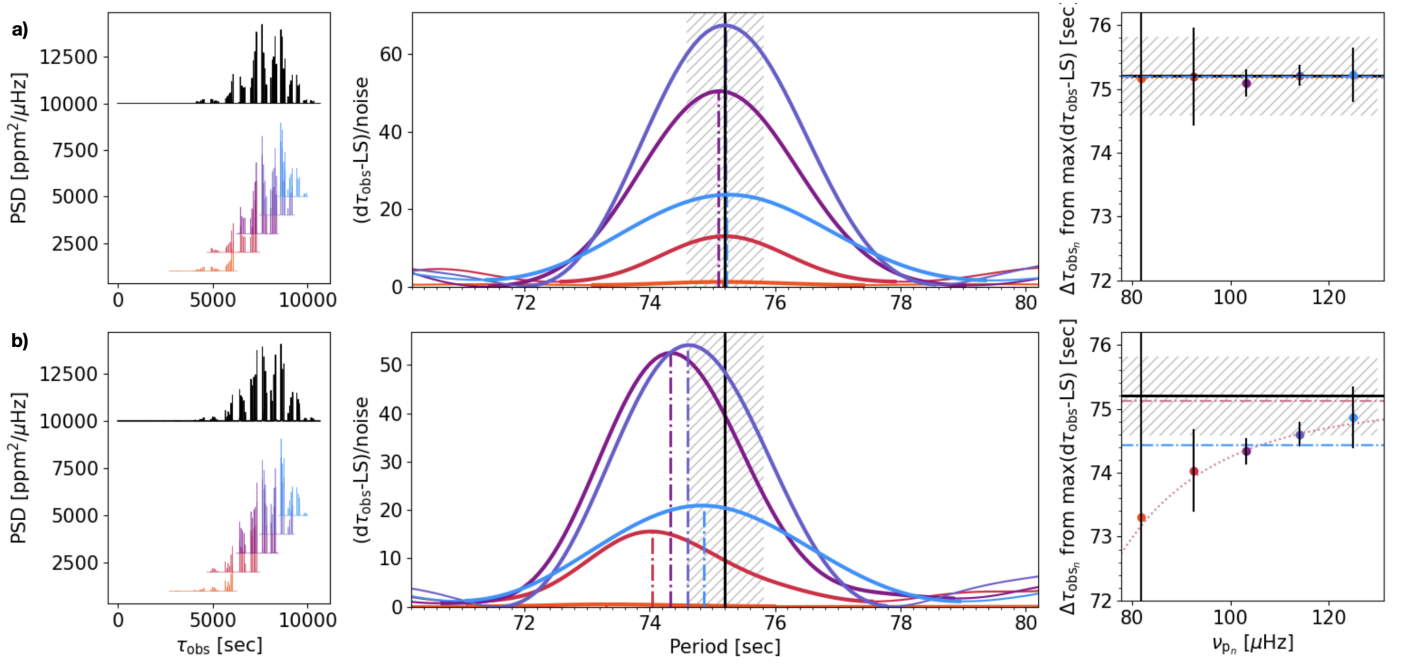


**Fig. 5.** Method to retrieve  $\Delta\Pi_1$ . **a)** Non-rotating, non-magnetized model as in the first panel of Fig. 1. **b)** Non-rotating, magnetized model as in the third panel of Fig. 1. In each case, left panels represent the stretched PSD according to the  $d\tau_{\text{obs}}$  variable (Eq. 15). Subsamples centered around the  $p$ - $m$  modes with a width of  $2 - \Delta\nu$  are extracted and plotted in different colors below one another. Vertical positions are chosen so that data do not overlap too much, they are therefore arbitrary. Middle panels show a zoom around the dominant peak in the normalized  $d\tau_{\text{obs}} - \text{LS}$  periodogram associated with the different frequency ranges color-coded on left panels. Curves are thicker within the central peak for better visualization. Vertical dot-dashed lines indicate the measurement of  $\Delta\tau_{\text{obs}_n}$  on the various frequency ranges. Hatched areas indicate the typical uncertainty  $\delta(\Delta\Pi_1)_{\text{res}} = 0.6$  seconds on the measurement of  $\Delta\Pi_1$  from LS-based methods according to the study of Vrad et al. (2016), centered around  $\Delta\Pi_1 = 75.2$  sec (same in the right panels). In right panels such local measurements of  $\Delta\tau_{\text{obs}_n}$  are transferred as a function of the central  $p$ - $m$  frequencies. The black line indicates the true value of  $\Delta\Pi_1$  and the blue dash-dotted line indicates  $\Delta\tau_{\text{obs}}$ . In the bottom panel, the dotted pink curve is the result of the Bayesian fit of the  $\Delta\Pi_1 - \nu_{p_m}$  law according to Eq. 38, and the pink dash-dotted line indicates the measurement of  $\Delta\Pi_1$  obtained from the fitting process (see Table 1).

First, we perform a non-linear least-squares fit to the data points in the  $\Delta\tau_{\text{obs}_n} - \nu_{p_n}$  diagram, from which we obtain the following values:  $\Delta\Pi_1 = 75.11$  sec and  $\delta\nu_{\text{mag,g}} = 0.39 \mu\text{Hz}$ . Then, we use these values as priors for a Bayesian fitting on the same data points, by using the emcee python ensemble (see Appendix E for the details of the fit, Foreman-Mackey et al. 2019). The result of the Bayesian fit is represented by the dash-dotted pink curve in the lower right panel of Fig. 5. With this diagram, we offer a way of detecting the presence of magnetic fields affecting the frequency of  $g$ - $m$  modes. The continuous pink line indicates the value of  $\Delta\Pi_{1,\text{LS}}$  as estimated from the fit to the data with  $\delta(\Delta\Pi_{1,\text{over}})$  uncertainties (see Table 1). As discussed, it is lower than the true value of  $\Delta\Pi_1$  due to the  $\nu \approx \nu_{p_n}$  approximation. The error of  $\Delta\Pi_1$  for this specific simulated model is  $|\Delta\Pi_1 - \Delta\Pi_{1,\text{LS}}| / \Delta\Pi_1 < 0.01\%$ , within the typical error associated with classical methods (from  $\delta(\Delta\Pi_{1,\text{res}})$ ) as represented by the hatched area in the right panels of Fig. 5. Here,  $\delta\nu_{\text{mag,g}}$  is underestimated by about 6%. For consistency, we also perform the Bayesian fit by taking into account the resolution uncertainty defined by Eq. 13, and the corresponding results are reported in the last row of Table 1. The magnetic effect is underestimated by about 12% in this case, and the error on  $\Delta\Pi_1$  is slightly larger than when using  $\delta(\Delta\Pi_{1,\text{over}})$ . This larger departure from the true value of each parameter is expected, as a lot of weight is given to less significant measurements when using  $\delta(\Delta\Pi_{1,\text{res}})$ .

#### 4.6. Confidence in the magnetic detection

Even if the star is not magnetized, it is always possible to fit the magnetized function,  $\mathcal{F}$ , to the data, and to extract a small magnetic splitting value. However, such a measurement is probably not significantly better than a fit with  $B_0 = 0$ , which means that it is necessary to assess the robustness of any magnetic detection from the Bayesian fit. To do so, we compare the result of the magnetized fit (Eq. 38) and those from the fit of a non-magnetized "nested" model  $\mathcal{F}_0$  defined as:

$$\mathcal{F}_0(\Delta\Pi_1) : \nu_{p_n} \rightarrow \Delta\Pi_1. \quad (39)$$

To do so, we perform a likelihood-ratio chi-squared test to approve or reject the null hypothesis  $H_0$ : "The full model and the nested model fit the data equally well. Thus, the nested model should be used". We calculate the p-value for the null model using the  $\chi^2_{\text{df}=1}$  cumulative distribution function:

$$p = P[\chi^2_{\text{df}=1} > \lambda_{\text{LR}}], \quad (40)$$

with  $\lambda_{\text{LR}}$  the ratio of the log likelihoods:

$$\lambda_{\text{LR}} = 2 [\log \mathcal{L}(\mathcal{F}) - \log \mathcal{L}(\mathcal{F}_0)]. \quad (41)$$

The p-value defined in Eq. 40 is the probability that the null hypothesis is true. A p-value lower than 0.05 means that we can reject the null hypothesis and consider the star to be magnetized with a level of confidence of 95%. In the case of the artificial magnetized star studied in Sect. 4.5, the p-value is  $< 0.001$ .

**Table 1.** Comparison of the performances of the  $\tau_{\text{obs}}$  method developed by Vrad et al. (2016) and the  $\pi_0$  fitting method from Sec. 4.5 in the case of a non-magnetized **a**) and a magnetized **b**) star, depending on the prescription chosen for uncertainties of  $\Delta\tau_{\text{obs}}$  measurements.

	True $\delta v_{\text{mag,g}}(v_{\text{max}})$ [ $\delta f_{\text{res}}$ ]	$\delta v_{\text{mag,g}}(v_{\text{max}})$ [ $\delta f_{\text{res}}$ ]	Uncertainty [ $\delta f_{\text{res}}$ ]	$\Delta\Pi_{1,\text{LS}}$ [sec]	Uncertainty [sec]	p-value
<b>a)</b> $\tau_{\text{obs}}$ method	0	$\emptyset$	$\emptyset$	75.19	$\delta(\Delta\Pi_{1,\text{res}}) = 0.61$	$\emptyset$
$\pi_0$ fitting method, $\delta(\Delta\Pi_{1,\text{over}})$	0	$\emptyset$	$\emptyset$	75.17	0.11	0.13
$\pi_0$ local fitting method, $\delta(\Delta\Pi_{1,\text{res}})$	0	$\emptyset$	$\emptyset$	75.18	0.27	1
<b>b)</b> $\tau_{\text{obs}}$ method	50	$\emptyset$	$\emptyset$	74.43	$\delta(\Delta\Pi_{1,\text{res}}) = 0.61$	$\emptyset$
$\pi_0$ local fitting method, $\delta(\Delta\Pi_{1,\text{over}})$	50	47	32	75.13	0.45	<0.001
$\pi_0$ fitting method, $\delta(\Delta\Pi_{1,\text{res}})$	50	44	22	75.12	0.53	<0.001

We, therefore, reject the null hypothesis and confirm the detection of magnetism from the LS method. In the case of the non-magnetized star, the p-value is above 0.05, therefore, the null hypothesis should not be rejected and the nested non-magnetic model ought to be considered. We confirm the non-detection of magnetism in the artificial non-magnetized star.

## 5. Results and discussion

The bottom panel of Fig. 4 presents the  $d\tau_0$ -LS periodogram computed when using the output of the fitting process:  $\Delta\Pi_1 = 75.13$  sec and  $\delta v_{\text{mag,g}} = 0.38 \mu\text{Hz}$ . As demonstrated by the comparison of top and bottom panels, we are able to largely reduce the error committed from the  $d\tau_{\text{obs}}$  method on the measurement of  $\Delta\Pi_1$  when the star is magnetized (as also reported on Table 1). The new measurement of  $\Delta\Pi_{1,\text{LS}}$  from this "observational"  $d\tau_0$ -LS periodogram is 75.15 sec (typical  $\delta(\Delta\Pi_{1,\text{res}}) = 0.6$  sec), coherent with the value resulting from the fit, and close to the true value of 75.2 seconds. The skewness of the dominant peak has also been largely reduced from 0.39 to 0.06 (see Appendix C for more details about the skewness of the dominant peak).

### 5.1. Detectability of the magnetic field through local $\Delta\Pi_1$ measurements

The fitting method presented in Sec. 4.5 relies on local measurements of  $\Delta\tau_{\text{obs}}$ , which have intrinsic uncertainties given by Eq. 14. The  $1/\nu^3$  signature of the magnetic frequency splitting might not emerge significantly from the method described in Sect. 2.1.4, with a p-value higher than about 0.05. This might happen when the ratio  $AB_0^2/\nu^3$  leads to magnetic signature on the order of only a few frequency resolutions or less when the signal to noise ratio in the spectrum leads to large  $\delta(\Delta\nu_{\text{over}})$  uncertainties or if the amplitude of the magnetized dipolar modes is also suppressed by the internal magnetic field (e.g., Fuller et al. 2015; Loi & Papaloizou 2017). To get more confidence in an eventual magnetic detection, we aimed to select stars combining a significant skewness in the dominant peak in the  $d\tau_{\text{obs}}$ -LS periodogram with a strong variation of the  $\Delta\tau_{\text{obs}}$  measurements with the frequency leading to a low p-value during the fitting process.

### 5.2. Confusion with other sources of frequency shifts

As extensively discussed in Bugnet et al. (2021), known sources of frequency perturbation do not produce signatures that resemble magnetic effects:

**Latitudinal differential rotation** produces perturbations that are typically smaller than the frequency resolution (De-

heuvels et al. 2017). Therefore, they are neglected in this study.

**Second-order rotational effects** As the star rotates, second-order and higher order asymmetric rotational perturbations of the centrifugal and Coriolis accelerations affect the perfectly-symmetric first-order rotational frequency pattern (Dziembowski & Goode 1992; Suárez et al. 2006). Deheuvels et al. (2017) demonstrated that the observed rotation rates on the RGB (Gehan et al. 2018) are too low for second-order rotational effects to significantly modify the frequency pattern of RGB stars.

**Structural glitches.** Sharp structural variations located in the deep layers of stars (hereafter, "glitches") are known to modify the frequency of mixed modes (Cunha et al. 2015). As a result, the observed period spacing of mixed modes can be affected by the structure of the star and strongly vary with the frequency. The study of Cunha et al. (2015), which focuses on the presence of glitches on the RGB shows that such processes arise mostly during very short events such as the RGB luminosity bump, at the early phases of helium core burning, as well as at the asymptotic giant branch bump. An asymmetric rotational triplet due to buoyancy glitches is then expected, caused by strong chemical gradients generated by the first dredge-up and left behind by the retreating envelope (Cunha et al. 2015, 2019; Jiang et al. 2020). Mosser et al. (2018) demonstrate that KIC 3216736 is the only RG among the 200 studied that presents buoyancy glitches. As a consequence, glitches are not a concern for the very large fraction of observed RG and this effect is neglected in the rest of our study. We point out that the search for magnetic fields according to the method described in this work should be carefully carried out on stars away from these evolutionary stages to avoid false detections.

**Near-degeneracy effects** result from the combination of rotation and mode mixing (Dziembowski & Goode 1992; Suárez et al. 2006). We refer to the complete study of Deheuvels et al. (2017) for the theoretical development of near-degeneracy effects on the asymmetry of rotational multiplets. These authors demonstrated that near-degeneracy effects should be taken into account when studying the frequency pattern along the RGB. However, the near degeneracy effect does not produce a pattern varying in  $1/\nu^3$  as magnetism does. For this reason, near-degeneracy effects should, in most cases, not be confused with a magnetic detection. We also emphasize the fact that near-degeneracy effects produce larger asymmetry measurements for larger order  $\ell$ , as opposed to magnetic effects (Bugnet et al. 2021), which adds a powerful diagnostic to disentangle the two mechanisms. The full comparison of near degeneracy effects and

magnetic signature is the object of the study by (Ong et al. 2022).

### 5.3. The $\Delta\Pi_1$ - $\Delta\nu$ diagram: Impact of the mass

Representing the observed  $\Delta\Pi_1$  values versus asteroseismic  $\Delta\nu$  is a powerful visualization tool to disentangle stars from the RGB and from the red clump, as  $\Delta\Pi_1$  is strongly modified during the transition. When focusing on the RGB, Vrad et al. (2016) noticed a dependency of the  $\Delta\Pi_1$  value on stellar mass. Indeed, an intermediate-mass RGB exhibits a greater  $\Delta\nu$  value than a low-mass star at fixed  $\Delta\Pi_1$ . It has been interpreted as the result of the difference in the density profile as observed from simulations (Stello et al. 2013), because intermediate-mass stars are more dense than low-mass stars at given stellar core properties (fixed  $\Delta\Pi_1$ ).

It is, however, also possible to reverse the scenario: intermediate-mass RG with ( $1.3M_\odot < M_\star < 1.6M_\odot$ ) present  $\Delta\Pi_1$  values that are slightly lower than low-mass RG ( $0.8M_\odot < M_\star < 1.3M_\odot$ ) at fixed  $\Delta\nu$ . As demonstrated in our study, non-detected internal stable magnetic fields might have artificially biased the measurements of the  $\Delta\Pi_1$  of intermediate-mass stars towards lower values. The mass dependency observed by Vrad et al. (2016) on the RGB could therefore also fully or partially artificially result from (undetected) magnetic fields inside intermediate-mass stars. The  $\Delta\Pi_1$ - $\Delta\nu$  diagram might therefore be used to flag candidates for a search for internal magnetic fields.

## 6. Conclusion and perspectives

In this work, we investigate how magnetic fields impact the measurement of the gravity mode (g-mode) period spacing from asteroseismic data of stars on the RGB and how such a measurement might allow us to detect the presence of buried magnetic fields inside the radiative interior of evolved stars. We created artificial RG power spectral densities (PSD) from mixed-mode frequency patterns (Mosser et al. 2015) and we account for rotational (e.g., Gizon & Solanki 2003), and magnetic perturbations on mode eigenfrequencies (Bugnet et al. 2021; Mathis et al. 2021). By performing a Lomb-Scargle periodogram on the PSD and extracting the period associated with the peak of maximum amplitude, as done by Vrad et al. (2016), we evaluate the effect of magnetic fields on the estimation of  $\Delta\Pi_1$ .

We demonstrate that g-mode period-spacing estimates, directly measured from asteroseismic data following Vrad et al. (2016), might be biased towards lower values due to the presence of stable magnetic fields buried inside RGB stars (Bugnet et al. 2021). The shift of  $\Delta\Pi_1$  measurements due to magnetism is small enough ( $\sim 1\%$ ) for magnetic stars to blend in with non-magnetic stars when performing automatic measurements of period spacing. Magnetic stars might therefore be hidden among stars already studied in the past. In addition to  $\Delta\Pi_1$  being shifted by the presence of magnetic fields inside the radiative interior of RGs, we show that the shape of the dominant peak in the LS periodogram that facilitates this measurement is also affected. A large skewness of the dominant peak in the LS periodogram of the  $d\tau_{\text{obs}}$ -stretched PSD is a first step to flag candidate stars for an optimal search of internal magnetic field signatures. This study relies on a first-order perturbative analysis of the magnetic field effects on mixed-mode frequencies performed in Bugnet et al. (2021). The critical magnetic-field amplitude above which the

perturbative analysis is not valid has been estimated by Bugnet et al. (2021): the expected magnetic fields amplitudes inside stars on the RGB are of about 1000 times lower than this critical field. We therefore confirm that the perturbative analysis presented here is valid for stars evolving on the red giant branch.

In addition, due to the frequency dependency of the magnetic effect on mixed-mode frequencies (see Mathis et al. 2021), the  $\Delta\Pi_1$  measured from various nested frequency intervals from a same PSD are different. Indeed, low-frequency  $\Delta\Pi_1$  values are much lower than  $\Delta\Pi_1$  computed from high-frequency intervals, as the effect of magnetism is the strongest on low-frequency g-m modes. We therefore provide the correct stretching function for magnetized stars, to account for magnetic effects when measuring the g-mode period spacing. We demonstrate that the variation of  $\Delta\Pi_1$  measurements with frequency allows to estimate the magnetic splitting as defined in Bugnet et al. (2021) and Mathis et al. (2021) as well as to correct for the measured value of  $\Delta\Pi_1$ .

We combine theoretical prescriptions with realistic simulations of asteroseismic observations to construct the first magnetic detection method based on the period spacing of mixed modes. This study opens the way for an extensive search of magnetic fields inside evolved stars with solar-like oscillations. Due to the known effect of magnetic fields on mixed-mode frequencies from Bugnet et al. (2021), the magnetic signature on local measurements of the period spacing of g-modes investigated here should not get mistaken for another known physical process also leading to frequency shifts (e.g., latitudinal differential rotation, centrifugal effects, glitches, near-degeneracy effects). Such a detection of magnetic-field signatures from the measurement of the period spacing of g-modes can then be inverted to get an estimate of the radial magnetic-field strength inside RGs following Mathis et al. (2021), as it is already possible for the internal rotation (e.g., Deheuvels et al. 2017, 2020). Our methodology is well-suited for stars observed with low-inclination angles or observed pole-on, as it is based on azimuthal order  $m = 0$  components to avoid additional signatures in the LS periodogram resulting from the distinct periodicity of  $m = \pm 1$  modes. As long as the magnetic-field amplitude remains moderate, the method presented here can be applied even if the field is inclined inside the star (see Appendix F). From the statistics on the amplitudes of oscillations on the RGB (e.g. Stello et al. 2016a), intermediate-mass stars seems more likely to host strong magnetic fields than low-mass stars during the RGB. There are a few stars in the study of Gehan et al. (2020) that are observed with low-inclination angles, with a mass above 1.3 solar masses, and that present a rather low value of  $\Delta\Pi_1$  from the study of Vrad et al. (2016). The detection of magnetic fields inside these stars is out of the scope of this paper and its focus on methodology, but we are able to identify these stars as the best sample for the search of buried magnetic fields. The observational search is made possible thanks to the theoretical progress made in this study. Such a detection would be game-changing for improving the understanding of all stars of low and intermediate mass, as they are described as non-magnetic bodies in current stellar evolution models. The presence of strong internal magnetic fields inside the radiative interior of stars along their evolution would modify stellar age estimates and would thus affect many astrophysical areas – from planet habitability studies to galacto-archeology (Rauer et al. 2014; Chaplin et al. 2020).

*Acknowledgements.* The author thanks S. Mathis, R.A. García, S. Mathur, C. Aerts, E. Corsaro, J. Fuller and M. Cantiello for very useful discussions. The author thanks the referee for their valuable time in reviewing the manuscript

and providing suggestions for improvement. This research was supported in part by the National Science Foundation under Grant No. NSF PHY-1748958. This research made use of Astropy,<sup>2</sup> a community-developed core Python package for Astronomy (Robitaille et al. 2013; Price-Whelan et al. 2018).

## References

- Abramowitz, M. & Stegun, I. 1972, *Handbook of Mathematical Functions* (New York: Dover)
- Acevedo-Arreguin, L. A., Garaud, P., & Wood, T. S. 2013, *Monthly Notices of the Royal Astronomical Society*, 434, 720
- Aerts, C. 2021, *Reviews of Modern Physics*, 93, 015001
- Aerts, C., Mathis, S., & Rogers, T. M. 2019, *Annual Review of Astronomy and Astrophysics*, 57, 35
- Akgün, T., Reisenegger, A., Mastrano, A., & Marchant, P. 2013, *Monthly Notices of the Royal Astronomical Society*, 433, 2445
- Arlt, R. & Weiss, N. 2014, *Space Science Reviews*, 186, 525
- Augustson, K. C., Brun, A. S., & Toomre, J. 2019, *The Astrophysical Journal*, 876, 83
- Barker, A. J., Jones, C. A., & Tobias, S. M. 2019, *Monthly Notices of the Royal Astronomical Society*, 487, 1777
- Beck, P. G., Bedding, T. R., Mosser, B., et al. 2011, *Science*, 332, 205
- Beck, P. G., Hambleton, K., Vos, J., et al. 2014, *Astronomy and Astrophysics*, 564, A36
- Beck, P. G., Montalbán, J., Kallinger, T., et al. 2012, *Nature*, 481, 55
- Bedding, T. R., Mosser, B., Huber, D., et al. 2011, *Nature*, 471, 608
- Belkacem, K., Marques, J. P., Goupil, M. J., et al. 2015, *Astronomy and Astrophysics*, 579, A30
- Benomar, O., Belkacem, K., Bedding, T. R., et al. 2014, *The Astrophysical Journal*, 781, L29
- Borucki, W., Koch, D., Batalha, N., et al. 2008, *Proceedings of the International Astronomical Union*, 4, 289
- Braithwaite, J. 2006, *Astronomy and Astrophysics*, 453, 687
- Braithwaite, J. 2007, *Astronomy and Astrophysics*, 469, 275
- Braithwaite, J. 2008, *Monthly Notices of the Royal Astronomical Society*, 386, 1947
- Braithwaite, J. 2009, *Monthly Notices of the Royal Astronomical Society*, 397, 763
- Braithwaite, J. & Nordlund, A. 2006, *Astronomy and Astrophysics*, 450, 1077
- Braithwaite, J. & Spruit, H. C. 2004, *Nature*, 431, 819
- Brun, A. S. & Browning, M. K. 2017, *Living Reviews in Solar Physics*, 14, 1
- Brun, A. S. & Zahn, J. P. 2006, *Astronomy and Astrophysics*, 457, 665
- Bugnet, L., Prat, V., Mathis, S., et al. 2021, *Astronomy and Astrophysics*, 650, A53
- Buysschaert, B., Beck, P. G., Corsaro, E., et al. 2016, *Astronomy and Astrophysics*, 588, A82
- Ceillier, T., Eggenberger, P., García, R. A., & Mathis, S. 2012, *Astronomische Nachrichten*, 333, 971
- Chaplin, W. J., Serenelli, A. M., Miglio, A., et al. 2020, *Nature Astronomy*, 4, 383
- Corsaro, E., Stello, D., Huber, D., et al. 2012, *Astrophysical Journal*, 757, 190
- Cunha, M. S., Avelino, P. P., Christensen-Dalsgaard, J., et al. 2019, *Monthly Notices of the Royal Astronomical Society*, 490, 909
- Cunha, M. S., Stello, D., Avelino, P. P., Christensen-Dalsgaard, J., & Townsend, R. H. 2015, *Astrophysical Journal*, 805, 127
- Deheuvels, S., Ballot, J., Eggenberger, P., et al. 2020, *Astronomy and Astrophysics*, 641, A117
- Deheuvels, S., Brandão, I., Silva Aguirre, V., et al. 2016, *Astronomy and Astrophysics*, 589, A93
- Deheuvels, S., Doğan, G., Goupil, M. J., et al. 2014, *Astronomy and Astrophysics*, 564, A27
- Deheuvels, S., García, R. A., Chaplin, W. J., et al. 2012, *The Astrophysical Journal*, 756, 19
- Deheuvels, S., Ouazzani, R. M., & Basu, S. 2017, *Astronomy and Astrophysics*, 605, A75
- Di Mauro, M. P., Ventura, R., Cardini, D., et al. 2016, *The Astrophysical Journal*, 817, 65
- Donati, J.-F. & Landstreet, J. 2009, *Annual Review of Astronomy and Astrophysics*, 47, 333
- Duez, V. & Mathis, S. 2010, *Astronomy and Astrophysics*, 517, A58
- Dupret, M. A., Belkacem, K., Samadi, R., et al. 2009, *Astronomy and Astrophysics*, 506, 57
- Dziembowski, W. A. & Goode, P. R. 1992, *The Astrophysical Journal*, 394, 670
- Eggenberger, P. 2015, *Astrophysics and Space Science Proceedings*, 39, 33
- Eggenberger, P., Buldgen, G., & Salmon, S. J. A. J. 2019a, *Astronomy & Astrophysics*, 626, L1
- Eggenberger, P., Deheuvels, S., Miglio, A., et al. 2019b, *Astronomy & Astrophysics*, 621, A66
- Eggenberger, P., Haemmerlé, L., Meynet, G., & Maeder, A. 2012, *Astronomy and Astrophysics*, 539, A70
- Eggenberger, P., Hartogh, J. W. d., Buldgen, G., et al. 2019c, *Astronomy and Astrophysics*, 631, L6
- Emeriau-Viard, C. & Brun, A. S. 2017, *The Astrophysical Journal*, 846, 8
- Foreman-Mackey, D., Farr, W., Sinha, M., et al. 2019, *Journal of Open Source Software*, 4, 1864
- Fuller, J., Cantiello, M., Stello, D., Garcia, R. A., & Bildsten, L. 2015, *Science*, 350, 423
- Fuller, J., Lecoanet, D., Cantiello, M., & Brown, B. 2014, *Astrophysical Journal*, 796, 17
- Fuller, J., Piro, A. L., & Jermyn, A. S. 2019, *Monthly Notices of the Royal Astronomical Society*, 485, 3661
- García, R. A. & Ballot, J. 2019, *Asteroseismology of solar-type stars*
- García, R. A., Pérez Hernández, F., Benomar, O., et al. 2014, *Astronomy and Astrophysics*, 563, A84
- Gehan, C., Mosser, B., Michel, E., & Cunha, M. S. 2020, *Astronomy and Astrophysics*, 645, A124
- Gehan, C., Mosser, B., Michel, E., Samadi, R., & Kallinger, T. 2018, *Astronomy and Astrophysics*, 616, A24
- Gizon, L. & Solanki, S. K. 2003, *The Astrophysical Journal*, 589, 1009
- Goode, P. R. & Thompson, M. J. 1992, *The Astrophysical Journal*, 395, 307
- Gough, D. O. & Thompson, M. J. 1990, *Monthly Notices of the Royal Astronomical Society*, 242, 25
- Goupil, M. J., Mosser, B., Marques, J. P., et al. 2013, *Astronomy and Astrophysics*, 549, A75
- Hekker, S., Elsworth, Y., Basu, S., & Bellinger, E. 2017, in *EPJ Web of Conferences*, Vol. 160
- Jiang, C., Cunha, M., Christensen-Dalsgaard, J., & Zhang, Q. 2020, *Monthly Notices of the Royal Astronomical Society*, 495, 621
- Kiefer, R. & Roth, M. 2018, *The Astrophysical Journal*, 854, 74
- Kissin, Y. & Thompson, C. 2015, *ApJ*, 809, 108
- Kuszlewicz, J. S., Chaplin, W. J., North, T. S. H., et al. 2019, *MNRAS*, 488, 572
- Landstreet, J. D. & Mathys, G. 2000, *A&A*, 359, 213
- Lebreton, Y., Goupil, M. J., & Montalbán, J. 2014, in *EAS Publications Series*, Vol. 65 (EDP Sciences), 177–223
- Lecoanet, D., Vasil, G. M., Fuller, J., Cantiello, M., & Burns, K. J. 2017, *Monthly Notices of the Royal Astronomical Society*, 466, 2181
- Loi, S. T. 2020, *Monthly Notices of the Royal Astronomical Society*, 496, 3829
- Loi, S. T. 2021, *MNRAS*, 504, 3711
- Loi, S. T. & Papaloizou, J. C. B. 2017, *Monthly Notices of the Royal Astronomical Society*, 3225, 3212
- Lomb, N. R. 1976, *Astrophysics and Space Science*, 39, 447
- MacGregor, K. B. & Cassinelli, J. P. 2003, *The Astrophysical Journal*, 586, 480
- Maeder, A. & Meynet, G. 1996, *A&A*, 313, 140
- Maeder, A. & Zahn, J.-P. 1998, *A&A*, 334, 1000
- Markey, P. & Tayler, R. 1973, *Monthly Notices of the Royal Astronomical Society*, 63, 77
- Marques, J. P., Goupil, M. J., Lebreton, Y., et al. 2013, *Astronomy and Astrophysics*, 549, A74
- Mathis, S. 2013, in *LNP*, Vol. 865, 23–47
- Mathis, S., Bugnet, L., Prat, V., et al. 2021, *Astronomy and Astrophysics*, 647, A122
- Mathis, S., Palacios, A., & Zahn, J. P. 2004, *Astronomy and Astrophysics*, 425, 243
- Mathis, S., Prat, V., Amard, L., et al. 2018, *Astronomy and Astrophysics*, 620, A22
- Mathis, S. & Zahn, J. P. 2004, *Astronomy and Astrophysics*, 425, 229
- Mestel, L. & Weiss, N. 1987, *Monthly Notices of the Royal Astronomical Society*, 226, 123
- Mosser, B. & Appourchaux, T. 2009, *Astronomy and Astrophysics*, 508, 877
- Mosser, B., Barban, C., Montalbán, J., et al. 2011, *Astronomy and Astrophysics*, 532, A86
- Mosser, B., Belkacem, K., Pinçon, C., et al. 2017a, *Astronomy and Astrophysics*, 598, A62
- Mosser, B., Belkacem, K., & Vradar, M. 2013, *EAS Publications Series*, 63, 137
- Mosser, B., Benomar, O., Belkacem, K., et al. 2014, 572, L5
- Mosser, B., Elsworth, Y., Hekker, S., et al. 2012a, *Astronomy and Astrophysics*, 537, A30
- Mosser, B., Gehan, C., Belkacem, K., et al. 2018, *Astronomy and Astrophysics*, 618, A109
- Mosser, B., Goupil, M. J., Belkacem, K., et al. 2012b, *Astronomy and Astrophysics*, 548, A10
- Mosser, B., Goupil, M. J., Belkacem, K., et al. 2012c, *Astronomy and Astrophysics*, 540, A143

<sup>2</sup> <http://www.astropy.org>



- Mosser, B., Pinçon, C., Belkacem, K., Takata, M., & Vrad, M. 2017b, *Astronomy and Astrophysics*, 600, A1
- Mosser, B., Vrad, M., Belkacem, K., Deheuvels, S., & Goupil, M. J. 2015, *Astronomy and Astrophysics*, 584, A50
- Neiner, C., Mathis, S., Alecian, E., Emeriau, C., & Grunhut, J. 2015, *Proceedings of the International Astronomical Union*, 10, 61
- Ong, J., Bugnet, L., & Basu, S. 2022, *ApJ*, submitted
- Ouazzani, R.-M., Goupil, M. J., Dupret, M.-A., & Marques, J. P. 2013, *Astronomy & Astrophysics*, 554, A80
- Pinçon, C., Belkacem, K., Goupil, M. J., & Marques, J. P. 2017, *Astronomy and Astrophysics*, 605, A31
- Price-Whelan, A. M., Hogg, D. W., Rix, H.-W., et al. 2018, *The Astronomical Journal*, 156, 18
- Rauer, H., Catala, C., Aerts, C., et al. 2014, *Experimental Astronomy*, 38, 249
- Robitaille, T. P., Tollerud, E. J., Greenfield, P., et al. 2013, *Astronomy & Astrophysics*, 558, A33
- Scargle, J. D. 1982, *Astrophysical Journal*, 263, 835
- Shibahashi, H. & Aerts, C. 2000, *The Astrophysical Journal*, 531, L143
- Shultz, M. E., Wade, G. A., Rivinius, T., et al. 2019, *Monthly Notices of the Royal Astronomical Society*, 490, 274
- Spruit, H. C. 2002, *Astronomy and Astrophysics*, 381, 923
- Stello, D., Cantiello, M., Fuller, J., Garcia, R. A., & Huber, D. 2016a, *Publications of the Astronomical Society of Australia*, 33, 16
- Stello, D., Cantiello, M., Fuller, J., et al. 2016b, *Nature*, 529, 364
- Stello, D., Huber, D., Bedding, T. R., et al. 2013, *Astrophysical Journal Letters*, 765, L41
- Strugarek, A., Brun, A. S., & Zahn, J. P. 2011, *Astronomy and Astrophysics*, 532, A34
- Suárez, J. C., Goupil, M. J., & Morel, P. 2006, *Astronomy and Astrophysics*, 449, 673
- Takata, M. & Shibahashi, H. 1994, *Publications of the Astronomical Society of Japan*, 46, 301
- Talon, S. & Charbonnel, C. 2008, *A&A*, 482, 597
- Talon, S. & Zahn, J. P. 1997, *Astronomy & Astrophysics*, 317, 749
- Tassoul, M. 1980, *The Astrophysical Journal Supplement Series*, 43, 469
- Tayar, J., Beck, P. G., Pinsonneault, M. H., García, R. A., & Mathur, S. 2019, *The Astrophysical Journal*, 887, 203
- Tayler, R. 1973, *Monthly Notices of the Royal Astronomical Society*, 61, 365
- Tayler, R. 1980, *Monthly Notices of the Royal Astronomical Society*, 191, 151
- Townsend, R. H. & Teitler, S. A. 2013, *Monthly Notices of the Royal Astronomical Society*, 435, 3406
- Triana, S. A., Corsaro, E., De Ridder, J., et al. 2017, *Astronomy and Astrophysics*, 602, A62
- Vrad, M., Mosser, B., & Samadi, R. 2016, *Astronomy and Astrophysics*, 588, 1
- Zahn, J. 1992, *Astronomy and Astrophysics*, 265, 115
- Zahn, J. P., Brun, A. S., & Mathis, S. 2007, *Astronomy and Astrophysics*, 474, 145

## Appendix A: Mixed-mode height and linewidth

To create artificial RG power densities, we use the following prescriptions for mixed-mode amplitudes and linewidths. The linewidth of each pure pressure mode is approximated, following the empirical fit of mode linewidths from the MS to the RGB by Corsaro et al. (2012), as:

$$\Gamma_p \approx 1.39 \exp\left(\frac{T_{\text{eff}} - 5777}{604}\right). \quad (\text{A.1})$$

The height of a resolved acoustic dipolar mode  $H_{1p}$  observed by *Kepler* can be approximated by (Mosser et al. 2012a, 2017a):

$$H_{1p}^2 = \frac{H_{0p}^2}{1.54}. \quad (\text{A.2})$$

As modes are often not resolved in the PSD, a dilution factor is taken into account (Mosser et al. 2018) and  $H_{1p}$  becomes:

$$H_{1p} = \frac{\pi}{2} \frac{\Gamma}{\delta f_{\text{res}}} \frac{H_{0p}}{\sqrt{1.54}}, \quad (\text{A.3})$$

with  $\delta f_{\text{res}}$  as the frequency resolution in the PSD ( $\delta f_{\text{res}} \approx 0.008 \mu\text{Hz}$  for four-year observations with the *Kepler* satellite simulated in this work). It is not only the frequencies, but also the amplitudes ( $A = \frac{\pi}{2} \Gamma H$ ) and linewidths that are modified via the coupling with g-modes (Benomar et al. 2014; Belkacem et al. 2015), following:

$$\Gamma(\nu) = \Gamma_p (1 - \zeta(\nu)) \quad (\text{A.4})$$

and

$$A^2(\nu) = A_p^2 (1 - \zeta). \quad (\text{A.5})$$

In addition, amplitudes in the PSD are modulated by the inclination angle of the star compared to the line of sight  $i$ , following (e.g., Gehan et al. 2020):

$$A^2(\nu_{m=0}) \propto \cos^2(i) \quad (\text{A.6})$$

and

$$A^2(\nu_{m=\pm 1}) \propto \frac{1}{2} \sin^2(i). \quad (\text{A.7})$$

## Appendix B: Calculation of the unperturbed mixed-mode frequency from magnetized PSD

We rewrite the following expression:

$$\nu^4 - \nu_{\text{obs0}} \nu^3 + \frac{\zeta AB_0^2}{2} = 0. \quad (\text{B.1})$$

as

$$ax^4 + bx^3 + e = 0, \quad (\text{B.2})$$

by defining  $a = 1$ ,  $b = -\nu_{\text{obs0}}$ , and  $e = \frac{\zeta}{2} AB_0^2$ .

The general solution of this 4<sup>th</sup> order equation can be written as

$$\nu = f(\nu_{\text{obs0}}) = -\frac{b}{4a} + \frac{p_4}{2} + \frac{\sqrt{p_5 + p_6}}{2}, \quad (\text{B.3})$$

with

$$p_1 = 27b^2e,$$

$$p_2 = p_1 + \sqrt{-4(12ae)^3 + p_1^2},$$

$$p_3 = \frac{12ae}{3a\left(\frac{p_2}{2}\right)^{1/3}} + \frac{\left(\frac{p_2}{2}\right)^{1/3}}{3a},$$

$$p_4 = \sqrt{\frac{b^2}{4a^2} + p_3},$$

$$p_5 = \frac{b^2}{2a^2} - p_3,$$

$$p_6 = -\frac{b^3}{4p_4}.$$

## Appendix C: Skewness of the dominant peak in the $d\tau_{\text{obs0}}$ -LS periodogram

### C.1. Skewness measurement

By expressing  $p_{\text{peak}}$ , the array of length  $N$  periods corresponding to the peak with maximum amplitude in the LS periodogram and  $A_{\text{peak}}$  the corresponding amplitude in the LS periodogram, we can measure the Fisher-Pearson coefficient of skewness of the peak distribution as a function of its mean value  $\mu$  and standard deviation  $\sigma$  through:

$$S = \frac{\frac{1}{N} \left( \sum_{n=1}^N A_{\text{peak}_n} (p_{\text{peak}_n} - \mu)^3 \right)}{\sigma^3}. \quad (\text{C.1})$$

For the  $d\tau_{\text{obs}}$ -stretched PSD of the simulated star represented in the first panel of Fig. 4, the  $S$  value is about 0.39. When using the appropriate  $d\tau_0$ -stretching function via Eq. 35 the skewness is brought closer to zero (quasi-normal distribution), as  $S \approx 0.07$  in the middle panel of Fig. 4.

### C.2. Lombscargle periodograms

We use a Lombscargle periodogram instead of the classical periodogram based on Fourier transforms because the stretched spectrum is unevenly spaced in the  $\tau_{\text{obs}}$  variable. The Lombscargle periodogram is a non-linear operator. We therefore ensure that the skewness of the dominant peak in the  $\tau_{\text{obs}}$ -LS value measured for the magnetic model is indeed related to magnetism and not to a property of the LS periodogram. To do so, we perform a nearest neighbor resampling on the  $\tau_0$ -stretched PSD, by resampling the stretched PSD to the minimum period resolution in the stretched PSD. We then perform a periodogram of the resampled stretched PSD with the `scipy.signal.periodogram` Python function. First, we confirm that the measurement of  $\Delta\Pi_1$  from this periodogram is compatible with the measurement from the  $\tau_{\text{obs}}$ -LS periodogram, which confirms that using LS periodograms does not bias the measurement of  $\Delta\Pi_1$ . Second, the skewness of the dominant peak in the  $\tau_{\text{obs}}$  periodogram for the non-magnetized and magnetized models is respectively 0.02 and 0.45, which confirms that the skewness detected in the magnetized model in Section 4.3 is indeed due to magnetism and is independent of the use of the LS method.

## Appendix D: $d\pi_1$ -stretched PSD

We could try to do the analogous study carried out from Sec. 4 with  $m = 0$  modes by focusing on  $m = \pm 1$  oscillation modes instead. If the star is magnetized but not rotating,  $m = \pm 1$  modes overlap and the stretched period  $\pi_1$  can be defined as:

$$d\pi_1 = -\frac{1}{\zeta} \frac{dv_{\text{obs}}}{f_1(v_{\text{obs}})^2} \frac{1}{1 - 3\zeta \frac{AB_0^2}{f_1(v_{\text{obs}})^4}}, \quad (\text{D.1})$$

with  $f_1(v_{\text{obs}})$  as the solution for:

$$v^4 - v_{\text{obs}}v^3 + \zeta AB_0^2 = 0. \quad (\text{D.2})$$

However, if the star rotates,  $f_1$  has to be rewritten as  $f_{\pm 1}$  as it depends on the value of  $m$ , as the solution for:

$$v^4 - v_{\text{obs}\pm 1}v^3 + \zeta AB_0^2 \pm \zeta \delta v_{\text{rot}} = 0. \quad (\text{D.3})$$

When using  $\pi_1$  instead of  $\pi_0$ , we must include the effect of rotation as well in our calculation of  $\Delta\Pi_1$  when looking at  $m = \pm 1$  modes if the star is magnetized and shows rotational signatures. As rotation signature are very likely to emerge in most observed stars, we suggest that we always ought to base the measurement of  $\Delta\Pi_1$  inside magnetized stars on  $m = 0$  modes in the PSD.

## Appendix E: Bayesian fitting

This appendix presents the corner plot of the distribution of the  $\Delta\Pi_1$  and  $AB_0^2$  parameters ( $\mathcal{F}$  model from Eq. 38, see Fig. E.1) and  $\Delta\Pi_1$  only ( $\mathcal{F}_0$  nested model from Eq. 39, see Fig. E.2) from the Bayesian fitting process with the emcee python ensemble (Foreman-Mackey et al. 2019).

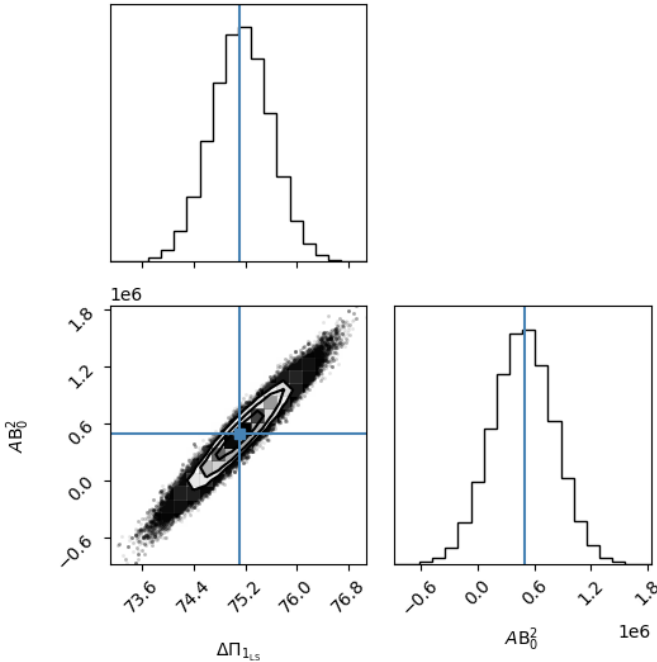


**Fig. E.1.** Corner plot showing the posterior distribution of  $\Delta\Pi_1$  and  $AB_0^2$  obtained from the magnetized Bayesian fit (Eq. 38). Blue lines indicate the starting values from the  $\chi^2$  fit.

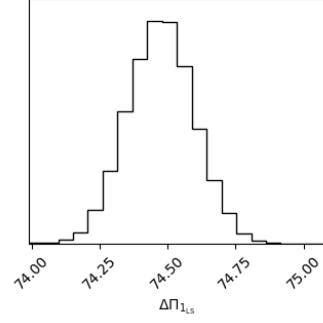


**Fig. E.2.** Corner plot showing the posterior distribution of  $\Delta\Pi_1$  obtained from the non-magnetized Bayesian fit (Eq. 39).

## Appendix F: Case of an inclined axisymmetric magnetic field

Our study is focused on the detectability of the magnetized signature defined by Eq. 24. This formulation approximates the effect of a stable, axisymmetric fossil field aligned with the rotation axis of the star, buried inside the radiative interior. However, spectropolarimetric observations of the surface of intermediate-mass stars on the MS show large-scale fossil magnetic fields inclined with respect to the rotation axis of the star (Landstreet & Mathys 2000; Shultz et al. 2019). As similar topologies are observed for stable fields at the surface of white dwarfs, it is necessary to extend the formalism to inclined stable magnetic fields. Loi (2021) investigates the effect of such an inclined field on the mixed-mode frequencies of RGs. This study unveils, in good agreement with previous theoretical works such as that of Goode & Thompson (1992), that an inclined magnetic field lifts the degeneracy of the azimuthal  $m$  order and generates a hyperfine structure in the frequency spectrum, made up of nine components in the case of dipolar modes. Such a signature might seem very different from the asymmetric triplet studied here. However, the relative amplitudes of the peaks constituting the hyperfine structure still result in an asymmetric-dominated pattern when the field is inclined and has moderate amplitude (Loi 2021). We therefore conclude that as long as the magnetic-field amplitude remains moderate (as expected from the conservation of the magnetic flux from pre-main and main sequence dynamo actions; see Bugnet et al. 2021, for more details), the method presented here can be applied even if the field is inclined inside the star.